HAL
open science

Dictyostelium lacking the single atlastin homolog Sey1 shows aberrant ER architecture, proteolytic processes and expansion of the Legionella -containing vacuole

Dario Hüsler, Bernhard Steiner, Amanda Welin, Bianca Striednig, A. Leoni Leoni Swart, Virginie Molle, Hubert Hilbi, François Letourneur

To cite this version:

Dario Hüsler, Bernhard Steiner, Amanda Welin, Bianca Striednig, A. Leoni Leoni Swart, et al.. Dictyostelium lacking the single atlastin homolog Sey1 shows aberrant ER architecture, proteolytic processes and expansion of the Legionella -containing vacuole. Cellular Microbiology, 2021, 23 (5), 10.1111/cmi.13318 . hal-03364992

HAL Id: hal-03364992

https://hal.science/hal-03364992v1

Submitted on 5 Oct 2021

HAL is a multi-disciplinary open access archive for the deposit and dissemination of scientific research documents, whether they are published or not. The documents may come from teaching and research institutions in France or abroad, or from public or private research centers.

L'archive ouverte pluridisciplinaire **HAL**, est destinée au dépôt et à la diffusion de documents scientifiques de niveau recherche, publiés ou non, émanant des établissements d'enseignement et de recherche français ou étrangers, des laboratoires publics ou privés.

Dictyostelium lacking the single atlastin homolog Sey1 shows aberrant ER architecture, proteolytic processes, and expansion of the *Legionella*-containing vacuole

Dario Hüsler[1], Bernhard Steiner[1#], Amanda Welin[2], Bianca Striednig[1], A. Leoni Swart[1], Virginie Molle[3], Hubert Hilbi[1*], François Letourneur[3*]

[1] Institute of Medical Microbiology, University of Zurich, Gloriastrasse 30, 8006 Zürich, Switzerland

[2] Division of Inflammation and Infection, Department of Biomedical and Clinical Sciences, Linköping University, 58185 Linköping, Sweden

[3] Laboratory of Pathogen Host Interactions, Université de Montpellier, CNRS, INSERM, Place Eugène Bataillon, Montpellier, 34095 cedex 5, France

Present address: [#]Institute for Molecular Bioscience, University of Queensland, Brisbane, Queensland 4072, Australia

Running title: *Dictyostelium* atlastin controls ER architecture and *Legionella* replication

Key words: Amoeba, atlastin, *Dictyostelium discoideum*, endocytic pathway, large GTPase, host-pathogen interaction, *Legionella pneumophila*, Legionnaires' disease, pathogen vacuole, unfolded protein response.

Abbreviations: Atlastin, ATL; Icm/Dot, intracellular multiplication/defective organelle trafficking; transmission electron microscopy, TEM; tunicamycin, TN; T4SS, type IV secretion system; unfolded protein response, UPR.

*Correspondence: hilbi@imm.uzh.ch; francois.letourneur@umontpellier.fr

Tel.: +41 (0)44 634 2650; +33 (0)46 714 4731

For Peer Review

ABSTRACT

Dictyostelium discoideum Sey1 is the single ortholog of mammalian atlastin 1-3 (ATL1-3), which are large homodimeric GTPases mediating homotypic fusion of endoplasmic reticulum (ER) tubules. In this study, we generated a *D. discoideum* mutant strain lacking the *sey1* gene and found that amoebae deleted for *sey1* are enlarged, but grow and develop similarly to the parental strain. The Δ*sey1* mutant amoebae showed an altered ER architecture, and the tubular ER network was partially disrupted without any major consequences for other organelles or the architecture of the secretory and endocytic pathways. Macropinocytic and phagocytic functions were preserved; however, the mutant amoebae exhibited cumulative defects in lysosomal enzymes exocytosis, intracellular proteolysis, and cell motility, resulting in impaired growth on bacterial lawns. Moreover, Δ*sey1* mutant cells showed a constitutive activation of the unfolded protein response pathway (UPR), but they still readily adapted to moderate levels of ER stress, while unable to cope with prolonged stress. In *D. discoideum* Δ*sey1* the formation of the ER-associated compartment harboring the bacterial pathogen *Legionella pneumophila* was also impaired. In the mutant amoebae, the ER was less efficiently recruited to the "*Legionella*-containing vacuole" (LCV), the expansion of the pathogen vacuole was inhibited at early stages of infection and intracellular bacterial growth was reduced. In summary, our study establishes a role of *D. discoideum* Sey1 in ER architecture, proteolysis, cell motility and intracellular replication of *L. pneumophila*.

1 INTRODUCTION

The endoplasmic reticulum (ER) is a pleiomorphic organelle composed of perinuclear membrane sheets and interconnected tubules extending towards the cell periphery (Shibata *et al.*, 2006, English *et al.*, 2009). This tubular network undergoes constant remodeling by

For Peer Review

homotypic fusion of ER tubules. Numerous proteins are required to form and maintain this dynamic ER network (Shibata *et al.*, 2009). Among them, the membrane-bound large GTPase atlastin (ATL) has been shown to mediate the homotypic fusion between tubules, ensuing the formation of three-way junctions and subsequent extensive reticulation of the ER network (Hu *et al.*, 2009, Orso *et al.*, 2009). In mammals, three ATL paralogs (ATL1-3) are selectively produced in different tissues. ATLs are highly conserved during evolution with only one single ortholog produced in yeast, plants or the amoeba *Dictyostelium discoideum* (named Sey1 in these different organisms) (Chen *et al.*, 2011, Anwar *et al.*, 2012, Zhang *et al.*, 2013, Steiner *et al.*, 2017). ATLs share a similar domain organization comprised of an N-terminal GTPase and a three-helix bundle (3HB), followed by two closely spaced predicted transmembrane (TM) segments and a C-terminal tail (CT). The role of ATLs in ER network formation is emphasized by the observation that mutations in the ATL genes were detected in the human neurological disorders hereditary spastic paraplegia (HSP) and hereditary sensory neuropathy (HSN), which are characterized by severe ER morphological defects (Salinas *et al.*, 2008, Guelly *et al.*, 2011, Fink, 2013, Fischer *et al.*, 2014, O'Donnell *et al.*, 2018). Furthermore, ATL gene deletion and overexpression of dominant-negative mutants result in defects of ER network formation (Rismanchi *et al.*, 2008, Hu *et al.*, 2009, Wang *et al.*, 2016, Zhao *et al.*, 2016).

Structural and biochemical studies indicate that upon GTP binding, the GTPase domains of ATL from two distinct ER tubules can form trans-homodimers, thus promoting membrane contact and fusion (Bian *et al.*, 2011, Byrnes *et al.*, 2011). The fusogenic properties of ATLs have been molecularly detailed by *in vitro* membrane fusion studies (Orso *et al.*, 2009, Bian *et al.*, 2011, Anwar *et al.*, 2012, Kim *et al.*, 2017) and crystal structure analysis (Bian *et al.*, 2011, Byrnes *et al.*, 2011, Liu *et al.*, 2012, Byrnes *et al.*, 2013, Liu *et al.*, 2015). In addition to ER dynamics, ATLs contribute to other cellular processes including lipid droplet biogenesis

For Peer Review

(Klemm *et al.*, 2013), mitochondrial lipid exchange (Voss *et al.*, 2012), membrane tethering (Krols *et al.*, 2018, Niu *et al.*, 2019), endosomal transport (Stefano *et al.*, 2015), inner nuclear membrane protein insertion (Pawar *et al.*, 2017), and selective autophagy (Liang *et al.*, 2018, Chen *et al.*, 2019).

Owing to numerous convenient genetic and biochemical tools, the amoeba *Dictyostelium discoideum* has been widely used as a model organism to study eukaryotic cell biology and host-pathogen interactions (Cardenal-Munoz *et al.*, 2017, Swart *et al.*, 2018). The phagocytic amoebae can engulf and digest bacteria as nutritional sources. However, some pathogenic bacteria avoid the degradative functions of *D. discoideum* and replicate inside this host cell. For instance, *Legionella pneumophila*, the causative agent of a severe pneumonia in humans termed Legionnaires' disease, induces the formation of a replication-permissive membrane-bound compartment called "*Legionella*-containing vacuole" (LCV) in the amoeba (Swart *et al.*, 2018).

The LCV biogenesis mechanism is comparable in human macrophages and amoeba (Gomez-Valero *et al.*, 2011, Al-Quadan *et al.*, 2012), and relies on the delivery of more than 300 different "effector" proteins into host cells by the bacterial Icm/Dot (Intracellular multiplication/defective organelle trafficking) type IV secretion system (T4SS). These effectors target and control key host cell processes including vesicular trafficking in the endocytic, secretory and retrograde pathways, lipid metabolism, translation, transcription, and apoptosis (Isberg *et al.*, 2009, Asrat *et al.*, 2014, Finsel *et al.*, 2015, Personnic *et al.*, 2016, Barlocher *et al.*, 2017, Steiner *et al.*, 2018a, Swart *et al.*, 2020a). The hijacking of host cell functions notably leads to the recruitment of ER-derived vesicles (Kagan *et al.*, 2004), as well as rough ER to LCVs (Swanson *et al.*, 1995, Robinson *et al.*, 2006, Weber *et al.*, 2014b, Weber *et al.*, 2018). The ER associating with LCVs might provide structural elements for

For Peer Review

pathogen vacuole formation and expansion, nutrients for intracellular growth, and/or camouflage from host cell defenses (Sherwood *et al.*, 2016).

ATL3 and Sey1 have been identified by proteomics in intact LCVs purified from *L. pneumophila*-infected macrophages or *Dictyostelium*, respectively (Hoffmann *et al.*, 2014). Recently, we validated the presence of ATL3/Sey1 on LCVs, and we revealed a functional role of this large GTPase for LCV formation (Steiner *et al.*, 2017). However, these studies were limited to an analysis of infected *D. discoideum* or isolated LCVs upon overproduction of a dominant negative Sey1 mutant, hampering further comprehensive studies. In order to assess the role of Sey1 for cellular processes and host-pathogen interactions, we adopted a genomic deletion strategy. In the present study, we uncovered the morphological and functional consequences of Sey1 genetic inactivation in *Dictyostelium* and further detailed Sey1 function(s) in the formation and expansion of the *Legionella* replicative vacuole.

2 RESULTS

2.1 Construction and basic characterization of *D. discoideum* Δ*sey1* cells

The only atlastin protein in *D. discoideum* is termed Sey1 (Steiner *et al.*, 2017). To analyze the function of Sey1, the corresponding gene was disrupted by insertion of the blasticidin selection marker by double homologous recombination (Figure 1a). This insertion left only a residual protein of 148 amino acids without any Sey1 functional domains. Several independent clones were analyzed and displayed identical phenotypes, which were complemented by transfection with the *sey1* coding sequence (see hereafter and data not shown).

When attached to standard plastic cell culture dishes, *D. discoideum* lacking Sey1 (Δ*sey1*) showed heterogeneously enlarged cell-surface size compared to Ax3 parental cells (2.2 times the normal median size; Figures 1b and 1c). Electric current exclusion measurements (CASY

For Peer Review

analyzer) further confirmed that Δ*sey1* cells had a greater diameter heterogeneity than Ax3 cells (mean diameters of 10.24 µm or 9.51 µm, respectively; Figure 1d). The *sey1* mutant amoebae were also frequently polynucleated (Figure 1e), suggesting a cytokinesis defect as described in fission yeast mutants affecting the cortical ER structure (Zhang *et al.*, 2010). Moreover, the relative growth rate of the Δ*sey1* strain was slightly reduced, and a plateau phase was reached at a lower cell density compared to Ax3 cells (Figure 1f). Upon starvation, aggregates and fruiting bodies were observed with genuine timing (Figure 1g). In summary, *D. discoideum* deleted for the *sey1* gene is viable and, compared to the parental strain, slightly enlarged and more frequently polynucleated, but develops largely normally. Moreover, the Δ*sey1* mutant strain grows slightly slower in axenic liquid medium.

2.2 *D. discoideum* lacking Sey1 shows aberrant ER morphology and dynamics

Since atlastin GTPases participate in the formation of the tubular ER network in other organisms, we examined the ER morphology in *D. discoideum* Δ*sey1* cells by confocal microscopy. In Ax3 parental cells, the ER-resident enzyme protein disulfide isomerase (PDI) localized both at the nuclear periphery and at interconnected ER tubules, which appeared to be extended throughout the entire cell towards the cell periphery (Figure 2a). In contrast, most Δ*sey1* cells showed clumps of PDI positive tubules at the cell periphery and a reduced interconnected ER tubule network. This altered ER morphology was identical in fixed and live cells producing the ER-resident reporter protein calnexin A-GFP (CnxA-GFP) (Figures 2b and 2c). Furthermore, ectopic production of GFP-Sey1 but not GFP-Sey1_K154A (GTPase defective mutant) in Δ*sey1* cells restored a normal ER morphology (Figure S1a), indicating that the GTPase activity of Sey1 is required to form and maintain a native ER network.

For Peer Review

Moreover, the ER-shaping protein reticulon (Rtnlc in *D. discoideum*), an interactor of Sey1, localized to ER tubules (but not to the perinuclear ER) in Ax3 and Δ*sey1* cells upon overproduction of an N-terminal GFP fusion protein, GFP-Rtnlc (Figure S1b). The ER-resident SNARE (soluble NSF attachment receptor) proteins Sec22b, Ufe1, and Use1 localized to ER tubules as well as the perinuclear ER in Ax3 and Δ*sey1* cells upon overproduction of the corresponding GFP fusion proteins (Figure S2). Taken together, Sey1 is required to establish normal ER architecture, but appears dispensable for the correct localization of Rtnlc and ER SNARE proteins.

The ER network is a highly dynamic structure, wherein tubules are constantly branching and fusing with each other (Schwarz *et al.*, 2016). To determine whether the absence of Sey1 might affect ER tubule dynamics, *D. discoideum* cells producing GFP-calnexin were analyzed by time-lapse video microscopy. While in the parental Ax3 strain, GFP-calnexin-positive ER tubules showed vivid dynamics, in live Δ*sey1* cells, GFP-calnexin-labeled nodular clumps were observed, which were mostly static. However, some faintly labeled ER tubules localized between the nucleus and the cell periphery and showed dynamics similar to that of Ax3 cells (Figure 2c, and Movies S1 and S2). These results indicate that tubule fusion and branching still occur in Δ*sey1* cells, however, to a much smaller extent.

Additional fluorescence microscopy analysis revealed that the morphology and distribution of other intracellular compartments was not altered in Δ*sey1* cells, and the architecture and dynamics of the microtubule cytoskeleton was fully conserved in the mutant cells (Figure S3, and Movies S3 and S4). Most importantly with regard to the functional analyses presented hereafter, the overall structure of endocytic compartments appeared unaffected in *D. discoideum* Δ*sey1* (Figure S3), and the subcellular distributions of PtdIns(3)*P* and PtdIns(4)*P*, hallmark phosphoinositide lipids of the endocytic and secretory pathway, respectively, appeared normal (Figures S4a and S4b). These conclusions were further supported by

For Peer Review

transmission electron microscopy (TEM) analysis which revealed no additional ultrastructural defects in Δ*sey1* cells besides the aberrant ER morphology observed by optical microscopy (Figure 2d). Taken together, the *D. discoideum* Δ*sey1* strain exhibits an aberrant ER tubule network characterized by clumps of PDI- and calnexin-positive tubules, but otherwise appears largely normal regarding cell organelle and cytoskeleton architecture and dynamics.

2.3 *D. discoideum* Δ*sey1* cells are impaired for growth on bacterial lawns

The reduced growth rate of Δ*sey1* cells in axenic liquid medium prompted us to examine their endocytic capacities. *D. discoideum* feeds on liquid medium by macropinocytosis. To evaluate this process, cells were incubated with fluorescent dextran for different periods of time, and uptake was measured by flow cytometry analysis. Dextran uptake occurred at a normal rate in Δ*sey1* cells, excluding that nutrient absorption is the growth-limiting step (Figure 3a). In *D. discoideum*, lysosomes mature into post-lysosomes, which eventually fuse with the plasma membrane and release their contents to the outside of the cells by exocytosis. In Δ*sey1* cells, the rate of exocytosis of fluorescent dextran showed a moderate but significant increase (51.3% of initial fluorescence retained after a chase period of 80 min in Δ*sey1* cells compared to 66.1% in Ax3 cells) (Figure 3b).

D. discoideum can ingest other sources of nutrients (e.g. bacteria) by phagocytosis. Surprisingly, Δ*sey1* cells could hardly grow on lawns of live (or even heat-killed) *Klebsiella pneumoniae*, unless the mutant strain was complemented by plasmid-borne GFP-Sey1 and myc-tagged Sey1 (Figures 3c and S5a). In contrast, the ectopic production of GFP-Sey1 in the parental Ax3 strain did not affect its growth on a *K. pneumoniae* lawn. The growth defect of Δ*sey1* was also observed with other bacterial strains, including *Escherichia coli* B/r and to a lesser extent with *Bacillus subtilis* and *Micrococcus luteus* (Figure 3d). Thus, the growth

For Peer Review

defect of *D. discoideum* Δ*sey1* occurs on lawns of different bacteria and is not restricted to particular Gram-negative or Gram-positive bacteria.

To grow on bacteria, *D. discoideum* has to bind, internalize, kill, and finally digest the bacterial cells. Interestingly, Δ*sey1* cells showed normal uptake of bacteria (*K. pneumoniae*) and fluorescent beads (Figures 3e and 3f), excluding any major defects in particle binding/recognition and uptake. Furthermore, identical bacteria killing efficiencies were observed for Ax3 and Δ*sey1* cells (Figure 3g). In summary, compared to the parental strain, Δ*sey1* cells show similar capacities for macropinocytosis, phagocytosis and exocytosis, but are severely impaired for growth on lawns formed by a range of bacteria. Together these results suggest that defective digestive functions might account for the growth defects of Δ*sey1* cells.

2.4 Lysosomal enzymes are hyper-secreted by Δ*sey1* cells

To evaluate the digestion of bacteria by *D. discoideum* Δ*sey1*, we first measured the activity of lysozymes, a family of enzymes responsible for the degradation of bacterial cell wall peptidoglycans (Lamrabet *et al.*, 2020). Two complementary assays revealed that Δ*sey1* cells exhibited only 75% of the intracellular activity of lysozymes measured in Ax3 cells (Figure 4a). Since exocytosis is increased in Δ*sey1* cells (Figure 3b), we hypothesized that lysosomal enzymes might be hyper-secreted, consequently decreasing their intracellular pool and impairing degradative functions of the lysosomes. To test this hypothesis, we measured the enzymatic activities of several lysosomal enzymes in cell and culture medium fractions separated after cultivation for 24 h. A higher percentage of α-mannosidase, cathepsin D (CtsD), and N-acetyl-glucosaminidase was secreted by Δ*sey1* compared to Ax3 cells, while the secretion of acid phosphatase was the same (Figures 4b and S5b). This secretion phenotype was largely reversed by the ectopic production of GFP-Sey1 (Figure 4b).

For Peer Review

In addition, we noticed that hypersecretion of lysosomal enzymes was associated with reduced total activities of α-mannosidase and CtsD inside the cells (Figure S5c). This decrease was caused by lower amounts of cellular lysosomal enzymes and not by reduction of their hydrolytic capacities when intracellularly retained. This was verified for CtsD by Western blot of whole cell lysates with an anti-CtsD antibody. Accordingly, in Δ*sey1* cells, a reduced amount of CtsD was observed in cell lysates, and this was partially compensated by ectopic production of GFP-Sey1 (Figures 4c and 4d).

We also noticed that the apparent molecular weight of CtsD in Δ*sey1* cells corresponds to the mature form of this enzyme (Figure 4c) (Journet *et al.*, 1999), suggesting that post-translational protein modifications occur normally in Δ*sey1* cells. This was further confirmed by the analysis of a highly glycosylated reporter protein, contact-site A (CsA) fused to transmembrane and cytoplasmic domains of SibA (Froquet *et al.*, 2012). This CsA-SibA chimeric protein showed the expected N- and O-glycosylation patterns in Δ*sey1* cells, reflecting a preserved genuine glycosylation process (Figure S5d).

Moreover, the acidification of endocytic compartments, which is required for optimal function of lysosomal enzymes, occurred at normal rates in Δ*sey1* cells, excluding any enzymatic activity defects due to non-optimal pH of degradative compartments (Figure S5e). Finally, total protein degradation in phagosomes was directly assessed by measuring proteolysis of DQ Green-BSA-coated beads at 1 h after cellular uptake. This assay revealed a 10% reduction of proteolysis in Δ*sey1* cells (Figure 4e). Together, these observations indicate that the intracellular retention of lysosomal enzymes is impaired in Δ*sey1* cells, consequently likely reducing the hydrolytic processing of nutrients required for optimal growth of the amoeba.

2.5 *D. discoideum* lacking *sey1* shows defective cell motility

For Peer Review

Upon growth on bacterial lawns, *D. discoideum* cells leave "grazed" regions and move towards more nutritive areas. To assess whether in addition to the impaired lysosomal degradation, a reduced cell motility could contribute to the growth defect of Δ*sey1* cells, random movement of individual cells seeded on a glass substrate in culture medium was recorded by time-lapse confocal microscopy (Figure 5a). Mutant Δ*sey1* cells showed a markedly reduced motility with a maximum distance from the initial position (D-max) of 23.0 ± 8.2 µm compared to 97.4 ± 21.4 µm for the Ax3 cells (Figure 5b). The ectopic production of GFP-Sey1 in Δ*sey1* cells partially restored motility (D-max = 68.6 ± 22.5 µm), in contrast to the GTPase defective mutant GFP-Sey1_K154A, which had almost no effect (D-max = 36.6 ± 15.9 µm). Moreover, while GFP-Sey1 did not affect the motility of Ax3 cells, the GFP-Sey1_K154A mutant protein strongly inhibited their motility (D-max = 51.5 ± 19.0 µm), indicating that the GTPase activity and/or dimerization of Sey1 is required for protein function, and consequently, cell motility. Since Δ*sey1* cells exhibited no major alteration in the organization of F-actin cellular protrusions (Figure S4c), other key players in cellular motility are likely affected by Sey1 deletion. In summary, dependent on its GTPase activity, Sey1 regulates the motility of *D. discoideum*.

2.6 Sey1 contributes to ER homeostasis in stressed cells

Atlastins in mammalian cells and RDH3 in plants have been shown to participate in the ER stress response (Lai *et al.*, 2014, Liang *et al.*, 2018, Chen *et al.*, 2019, Niu *et al.*, 2019). To test whether Sey1 adopts similar functions in *D. discoideum*, Δ*sey1* cells were incubated with tunicamycin (TN), a compound which induces ER stress and triggers the unfolded protein response (UPR) pathway (Dominguez-Martin *et al.*, 2018a, Dominguez-Martin *et al.*, 2018b). After 24 h of treatment the viability of Δ*sey1* was only slightly reduced compared to Ax3 cells (Figure 6a). However, this difference was dramatically amplified after 48 h and 72 h. After 48

For Peer Review

h, only 21.5% Δ*sey1* cells were alive compared to 69.2% Ax3 cells, and at 72 h the difference was also more than 3-fold. Phase contrast microscopy observations at 48 h further confirmed these results (Figure 6b).

Interestingly, the viability difference between Δ*sey1* and the parental Ax3 strain was dependent on the TN dose (Figure 6c). The viability of Δ*sey1* cells dropped to 45.9% at 125 ng/mL TN and reached a minimum of 20.2% viable cells at 1 µg/mL TN. In contrast, Ax3 parental cells as well as Δ*sey1* cell ectopically producing RFP-Sey1 showed only a mild reduction in viability (67.7% and 61.1% viable cells, respectively) even at the highest concentration of TN tested (1.5 µg/mL). Thus, Δ*sey1* cells manage to readily adapt to short-term ER stress, but exhibit strikingly reduced capacities to cope with prolonged ER stress.

To restore cellular homeostasis upon ER stress, cells increase protein degradation rates by several mechanisms, including the ubiquitin-dependent ERAD (ER-associated degradation) pathway and macroautophagy (hereafter referred to as autophagy) (Almanza *et al.*, 2019). To assess a role for Sey1 in ERAD, we first tested the production of CdcD (ERAD protein homologous to human VCP/p97 and yeast Cdc48) in response to TN (Figure 6d and 6e). In agreement with published results (Dominguez-Martin *et al.*, 2018b), CdcD production increased in Ax3 cells upon addition of TN for 24 h. A similar induction was observed in Δ*sey1* cells; however, the basal production of CdcD in untreated cells was higher in Δ*sey1* than in Ax3 cells. This result might reflect a constitutive activation of the ERAD pathway in mutant cells. In contrast, the basal production of PDI, a multifunctional ER-resident redox chaperone, was not enhanced in resting Δ*sey1* cell, whereas TN treatment resulted in identical induction of PDI production in Δ*sey1* and Ax3 cells, as expected for a treatment known to augment protein folding capacities (Figure 6d and 6e). In summary, compared to the parental Ax3 strain Δ*sey1* cells are more sensitive to ER stress.

For Peer Review

2.7 Intracellular replication and killing of *L. pneumophila* in Δ*sey1* cells

Intracellular replication of *L. pneumophila* occurs in ER-associated LCVs and implicates Sey1 (Steiner *et al.*, 2017). To test intracellular growth of *L. pneumophila* in *D. discoideum* Δ*sey1* cells, we used mCherry-producing bacteria and quantified fluorescence intensity (RFU) as well as the number of colony-forming units (CFU) (Figures 7a and S6a). In both assays, wild-type *L. pneumophila* showed a severe growth defect upon replication in Δ*sey1* cells. On the other hand, the *L. pneumophila* Δ*icmT* mutant strain was unable to replicate in the *D. discoideum* Ax3 or Δ*sey1* strain (Figure 7a), and killing (or survival) of Δ*icmT* bacteria was not different in *D. discoideum* Δ*sey1* compared to the parental strain Ax3 (Figure 7b). Taken together, *L. pneumophila* replicates less efficiently in Δ*sey1* compared to the parental strain, and hence, Sey1 promotes intracellular replication of *L. pneumophila*.

2.8 Recruitment of rough ER to LCVs is impaired in *D. discoideum* Δ*sey1* cells

Given the various defects of *D. discoideum* Δ*sey1* cells in ER morphology and dynamics, we sought to assess LCV formation in the mutant amoebae. In order to obtain high-resolution images of LCVs in *D. discoideum* Ax3 and Δ*sey1* cells, we used regular TEM (Figure 7c). Upon infection with wild-type *L. pneumophila*, rough ER was observed at 2 h p.i. and 8 h p.i. around LCVs in *D. discoideum* Ax3 and in Δ*sey1* cells producing plasmid-borne GFP-Sey1, but not in Δ*sey1* mutant cells. No ER accumulated around vacuoles harboring the avirulent *L. pneumophila* Δ*icmT* in any of these *D. discoideum* strains at any time, as has been observed previously with amoebae producing dominant-negative GFP-Sey1_K154A (Steiner *et al.*, 2018b). In summary, in agreement with the severe defect of Δ*sey1* cells regarding ER morphology and dynamics, LCVs harboring wild-type *L. pneumophila* are not decorated with rough ER in the mutant amoebae.

For Peer Review

2.9 PtdIns(4)*P*-positive LCVs in *D. discoideum* Δ*sey1* acquire ER less robustly

Next, we assessed LCV formation by confocal microscopy using dually labeled *D. discoideum* Ax3 or Δ*sey1* producing the PtdIns(4)*P*/LCV probe P4C-mCherry and the ER marker calnexin-GFP. Compared to the uninfected dually labeled Ax3 strain, in Δ*sey1* cells the ER was disorganized, fragmented and showed a vesicular organization (Figures 2b and S6b). This defective ER morphology was retained in *L. pneumophila*-infected Δ*sey1* cells and was particularly striking at early time points of infection (up to 8 h p.i.; Figure 8).

In general, LCVs formed by wild-type *L. pneumophila* in the Δ*sey1* mutant accumulated less calnexin-positive ER than LCVs in the parental strain Ax3, in particular at early time points during infection (2 h p.i.) (Figure 8a). These fluorescence microscopy observations validate the TEM data (Figure 7c). In the Δ*sey1* as well as in the Ax3 parental strain, the ER localized to LCVs not homogenously but in a rather patchy manner. Moreover, the PtdIns(4)*P*-positive limiting LCV membrane was formed in Δ*sey1* cells as well as the parental strain, and remained clearly visible throughout the infection (2 h - 48 h p.i.) (Figures 8, S6c, and S6d).

To quantify the recruitment of calnexin to PtdIns(4)*P*-positive LCVs in an unbiased and high-throughput manner, we used imaging flow cytometry (IFC). To this end, we infected the dually labeled *D. discoideum* strain producing P4C-mCherry and calnexin-GFP with mPlum-producing *L. pneumophila* (Figure 8b). The IFC colocalization score (see Materials and Methods) for the acquisition of calnexin-GFP to LCVs was then assessed. The calnexin-GFP colocalization score on LCVs formed by wild-type *L. pneumophila* increased during early time points of infection (1 h - 6 h p.i.) (Figure 8b), and was significantly lower in amoebae lacking Sey1. The calnexin-GFP colocalization score on LCVs decreased at later time-points (24 h - 48 h p.i.; Figure S6e). Finally, calnexin-GFP did not colocalize on Δ*icmT*-containing vacuoles in neither Ax3 or Δ*sey1* cells (data not shown), confirming that these LCVs do not

For Peer Review

acquire ER (Weber *et al.*, 2014b, Steiner *et al.*, 2017). In summary, quantitative data from IFC confirmed the confocal microscopy observations that Sey1 promotes the acquisition of ER by LCVs harboring wild-type *L. pneumophila*.

Following the same procedure, we also assessed the time-dependent colocalization score of P4C-mCherry on LCVs by IFC. The IFC colocalization score of P4C-mCherry on LCVs formed by wild-type *L. pneumophila* increased during early time points of infection (1 h - 6 h p.i.) (Figure 8b), while it decreased at later time points (24 h - 48 h p.i.) (Figure S6e). There was almost no difference in the P4C-mCherry colocalization score between infected *D. discoideum* Ax3 and Δ*sey1*. Hence, Sey1 appears dispensable for the acquisition of PtdIns(4)*P* to the LCV membrane. Finally, P4C-mCherry was not observed on vacuoles formed by Δ*icmT* mutant bacteria (data not shown), confirming that these LCVs do not undergo PI conversion and are not decorated with PtdIns(4)*P* (Weber *et al.*, 2014a, Steiner *et al.*, 2017). In summary, while the accumulation of calnexin-positive ER on LCVs in *D. discoideum* is dependent on Sey1, the acquisition of PtdIns(4)*P* at the limiting LCV membrane occurs independently of Sey1.

2.10 LCV expansion is delayed in *D. discoideum* Δ*sey1* cells

A hallmark of LCV maturation is its expansion to accommodate a growing number of vacuolar bacteria. Comparing the LCV expansion in *D. discoideum* Ax3 and Δ*sey1*, we found that while in the parental strain the PtdIns(4)*P*-positive limiting LCV membrane expanded, in Δ*sey1* cells the PtdIns(4)*P*-positive membrane remained rather tightly wrapped around the bacteria at early time points (2 h - 16 h p.i.) and only later expanded (24 h - 48 h p.i.) (Figures 8c, S6c, and S6d). These results indicate that Sey1 indeed promotes the expansion of the PtdIns(4)*P*-positive LCV membrane early during infection but appears dispensable at later stages of infection. The quantification of the LCV area revealed that at 2 h - 16 h p.i., LCVs

For Peer Review

in Δ*sey1* cells were approximately 1.5-fold smaller than in the parental strain (Figure 8d). At later time points (24 h - 48 h p.i.), the expansion defect disappeared, suggesting that Sey1 deletion only delays early LCV expansion (Figures 8c, 8d, S6c, and S6d). Taken together, infection of dually labeled *D. discoideum* producing the PtdIns(4)*P*/LCV probe P4C-mCherry and the ER marker calnexin-GFP revealed that in *D. discoideum* lacking Sey1 LCV expansion is delayed early during infection. Hence, Sey1 plays a crucial role for LCV maturation and intracellular replication of *L. pneumophila*.

3 DISCUSSION

3.1 *D. discoideum* Δ*sey1* amoebae show an abnormal ER architecture

D. discoideum deleted for Sey1 were shown here to display an abnormal ER network morphology, with disorganized clumps of ER tubules at the cell periphery, as reported for several organisms following ATL gene deletion (Rismanchi *et al.*, 2008, Hu *et al.*, 2009, Wang *et al.*, 2016, Zhao *et al.*, 2016). This morphological defect was only rescued by overexpression of Sey1 with a functional GTPase domain, consistent with the well-established ATL GTPase-dependent fusion of tubules leading to the formation of three-way junctions within tubules to create the cortical ER mesh. Unexpectedly, some ER branching still occurred in the absence of Sey1, indicating that Sey1-independent fusion events might partially compensate the loss of Sey1, thus ensuring cell viability. An alternative fusion pathway mediated by the ER SNAREs Ufe1p, Sec22p/Sec20p, Use1p and the tethering Dsl1 complex has been described in *S. cerevisiae* (Rogers *et al.*, 2014). Since *D. discoideum* orthologs of these SNARES still localized to the ER in the absence of Sey1, a similar SNARE-based fusion process might exist in this amoeba.

The stabilization of ER tubules is dependent on reticulon (Rtn) and Yop1p/DP1/REEP families of ER-shaping proteins that directly interact with ATLs (Hu *et al.*, 2009, Park *et al.*,

For Peer Review

2010). The ER-network formation requires a finely tuned balance between ATL-dependent tubule fusion and Rtn-mediated tubule curvature (Wang *et al.*, 2016). *D. discoideum* expresses only one Rtn ortholog (Rtnlc), and inhibition of Rtnlc functions by its deletion or overexpression had no obvious consequences on the shape of ER tubules (Figures S1b and S2c). The absence of defects in Δ*rtnlc* cells is consistent with the normal ER network morphology observed in Rtn1p and Rtn2p deleted yeast cells (Voeltz *et al.*, 2006). Moreover, the loss of RTN4a/b in mouse embryonic fibroblasts induces a reduction of ER tubulation (Jozsef *et al.*, 2014), and the overexpression of the reticulons results in tubule fragmentation (Wang *et al.*, 2016, Espadas *et al.*, 2019). This discrepancy suggests that besides Rtnlc, other ER-shaping proteins might stabilize tubules in *D. discoideum. PSI*-BLAST searches did not reveal any *D. discoideum* orthologs of DP1/Yop1/REEP proteins, and therefore, Δ*rtnlc* cells might advantageously allow the identification of new tubule curvature mechanisms or factors.

3.2 *D. discoideum* Δ*sey1* amoebae upregulate the UPR pathway

In mammalian cells, deletion of ATLs has been shown to induce the UPR pathway to limit ER stress due to the delay in ER exit of some cargo proteins (Niu *et al.*, 2019). Confirming this observation, we show here that Sey1 deletion caused the overexpression of the ERAD protein CdcC, indicative of a constitutively active UPR pathway. This possibly implies that the ER morphological defects in Δ*sey1* cells might interfere with proper cargo protein sorting or folding in the ER. Interestingly, we observed that Δ*sey1* cells were unable to cope with prolonged ER stress induced by tunicamycin. Besides the ERAD pathway, autophagy and ER phagy/reticulophagy have been shown to contribute to the cellular response to ER stress (Smith *et al.*, 2017, Song *et al.*, 2018, Stolz *et al.*, 2019, Wilkinson, 2019, Wilkinson, 2020). Hence, the selection of ER subdomains containing damaged or excess material is mediated by several specific ER-phagy receptors including atlastin (ATL3) (Chen *et al.*, 2019). Further

For Peer Review

studies will be required to assess whether autophagy and ER-phagy processes are altered in Δ*sey1* cells.

3.3 *D. discoideum* Δ*sey1* amoebae are defective for growth on bacterial lawns

D. discoideum Δ*sey1* cells had a marked growth defect when fed on bacteria and, to a lesser extent, on axenic liquid culture medium. Our results indicate that at least two cumulative defects in proteolysis and cell motility might account for these defective growth rates. First, we established that reduced proteolytic capacities in Δ*sey1* cells were correlated with impaired intracellular retention of lysosomal enzymes due to increased lysosomal exocytosis rates. In *D. discoideum*, lysosomes undergo several maturation steps to form post-lysosomes which eventually become competent to fuse with the plasma membrane to expel their content. Lysosomal exocytosis defects have been described in several *D. discoideum* mutants affecting lysosomal maturation before lysosome exocytosis (Charette *et al.*, 2007, Charette *et al.*, 2008, Carnell *et al.*, 2011). Since no noticeable lysosomal maturation defects were observed in Δ*sey1* cells, a hypothetical ER-dependent step in the exocytosis process might be altered in the absence of Sey1. For instance, the ER might provide key factors owing its close proximity to lysosomes at membrane contact sites (MCS) (Phillips *et al.*, 2016). The morphological defects of the peripheral ER network in Δ*sey1* cells might interfere with the formation, the location or even the function of these ER-lysosome MCS.

The growth defect on bacterial lawns might also be amplified by the reduced cell motility observed in Δ*sey1* cells. The ER network has been shown to maintain connections with the actin and microtubule cytoskeletons, both required for cell motility. Several ER proteins, such as CLIMP63, P180, REEP1, Sec61b, and STIM1 physically interact with microtubules (MTs) (Klopfenstein *et al.*, 1998, Ogawa-Goto *et al.*, 2007, Grigoriev *et al.*, 2008, Park *et al.*, 2010, Zhu *et al.*, 2018), whereas SYP73 recruits the actin cytoskeleton in *Arabidopsis* (Cao *et al.*,

For Peer Review

2016). A number of studies indicate that the ER can assist the cytoskeleton during organelle and cell motility. For instance, spastin, an ATPase with MT-severing activity regulating MT dynamics, has been shown to bind atlastin and REEP1 (Evans *et al.*, 2006, Sanderson *et al.*, 2006, Lee *et al.*, 2009, Park *et al.*, 2010), and its depletion affects the motility of Glioblastoma cells (Draberova *et al.*, 2011). Furthermore, in *Arabidopsis*, deletion of the atlastin-related protein RDH3 prevents ER streaming during cell expansion (Stefano *et al.*, 2014). Accordingly, the altered ER morphology of Δ*sey1* cells might hamper the proper mobilization of ER tubules to physically assist the cytoskeleton during cell migration.

In the context of host-pathogen interactions, phagocytes infected with *L. pneumophila* were impaired for cell and organelle motility (Rothmeier *et al.*, 2013, Swart *et al.*, 2020b). A family of RCC1 repeat containing *L. pneumophila* effectors has been shown to activate the small GTPase Ran, and consequently, stabilize MTs and promote cell and organelle motility. It is unknown whether *L. pneumophila* has evolved strategies to interfere with ER-associated motility functions.

3.4 *D. discoideum* Δ*sey1* amoebae restrict growth of *L. pneumophila*

Inside eukaryotic host cells, the facultative intracellular bacterium *L. pneumophila* establishes an ER-associated replication-permissive vacuole, the LCV. To this end, the pathogen employs a multi-step process, including ATL3/Sey1-dependent ER recruitment (Steiner *et al.*, 2017). Given the various defects of *D. discoideum* Δ*sey1* cells in ER morphology and dynamics, we assessed intracellular replication and LCV formation in the mutant amoebae. Indeed, Δ*sey1* cells restricted the intracellular growth of *L. pneumophila* but not the killing of an avirulent mutant strain (Figures 7a and 7b). TEM and confocal microscopy analyses as well as IFC revealed a disrupted ER morphology in Δ*sey1* cells and showed defective recruitment of ER to LCVs, which was successfully complemented by plasmid-borne production of GFP-Sey1

For Peer Review

(Figures 7c, 8a, and 8b). Moreover, confocal microscopy analysis using dually labeled *D. discoideum* producing in parallel the PtdIns(4)*P*/LCV probe P4C-mCherry and the ER marker calnexin-GFP revealed that the expansion of LCVs formed in Δ*sey1* cells was significantly delayed (Figures 8c and 8d).

These findings are in agreement with previous observations using *D. discoideum* producing a catalytically-inactive, dominant negative variant of Sey1 (Sey1_K154A), which was found to inhibit intracellular replication of *L. pneumophila*, as well as the decoration with ER, the expansion and the aggregation/fusion of LCVs (Steiner *et al.*, 2017, Steiner *et al.*, 2018a). In addition, the results reported in this study rule out off-target effects of Sey1_K154A, such as the formation of heterodimers with large GTPases other than Sey1. Indeed, the depletion by RNA interference of another large GTPase, the mitochondrial fission factor DNM1L (dynamin 1-like protein), has recently been shown to impair intracellular replication of *L. pneumophila* (Escoll *et al.*, 2017).

The mechanism underlying the role of Sey1 for LCV expansion is unknown. Sey1-catalyzed ER dynamics might promote the budding, trafficking and/or fusion of ER-derived vesicles, which interact with the pathogen vacuole (Kagan *et al.*, 2002), and thus, contribute to LCV maturation and expansion. Alternatively, the Sey1-catalyzed spatial vicinity of ER to the PtdIns(4)*P*-positive pathogen vacuole might foster the formation of MCSs, which promote lipid exchange and LCV expansion. Furthermore, our detailed analysis of the LCV maturation kinetics by confocal microscopy indicated that the expansion of LCVs in the Δ*sey1* cells was delayed only up to 16 h p.i. (Figures 8c and 8d). This defect appears to contribute to an overall inhibition of intracellular replication of *L. pneumophila* in *D. discoideum* lacking Sey1 (Figure 7a). The replication defect appeared to be more pronounced in Δ*sey1* amoebae (~3-fold decrease in replication) in comparison to the previously published defect caused by the overproduction of the dominant negative Sey1 variant, Sey1_K154A (~2-fold decrease in

For Peer Review

replication) (Steiner *et al.*, 2017). The reasons for a role of Sey1 in LCV expansion only at rather early time points of infection and LCV maturation are unclear (Figures 8c, 8d, and S6). Perhaps, fully functional ER architecture and dynamics are required only in the initial phase to provide structural elements for LCV formation and expansion, nutrients for intracellular growth, and/or protection from innate, host cell-autonomous defenses. Likely, the initial phase of infection with a pathogen determines the outcome of the pathogen-host relationship, i.e., that either the pathogen succeeds to establish a protective, replication-permissive niche, or the host cell manages to kill the intruder.

In conclusion, in the present study we have characterized a number of phenotypes of *D. discoideum* lacking Sey1. We showed that Δ*sey1* mutant amoebae are viable, exhibit defective ER morphology and dynamics, reduced proteolytic processes and cell migration, as well as impaired ER recruitment to LCVs, delay in pathogen vacuole expansion and reduced intracellular replication of *L. pneumophila*. The successful generation of *D. discoideum* Δ*sey1* mutant cells paves the way for further detailed characterization of the role of Sey1 in a variety of cellular processes as well as for pathogen vacuole formation and maturation of different, intracellular pathogens.

For Peer Review

4 EXPERIMENTAL PROCEDURES

4.1 Cell culture and *L. pneumophila* infections

Detailed information on cell lines and bacterial strains used is reported in the Table S1. *D. discoideum* strain Ax3 was grown at 22°C in HL5 medium or on lawns of live or heat-killed bacteria as previously reported (Alibaud *et al.*, 2008). For infections with *L. pneumophila*, *D. discoideum* Ax3 and Δ*sey1* mutant amoebae were cultivated in HL5 medium (ForMedium) at 23°C and transformed as previously described (Weber *et al.*, 2014a, Weber *et al.*, 2014b). Transformation of two constructs in parallel was performed to obtain dually-fluorescent

strains. Geneticin (G418, 20 µg/mL) and hygromycin (50 µg/mL) was supplemented when necessary.

L. pneumophila strains were grown for 3 days at 37°C on agar plates containing charcoal yeast extract (CYE), buffered with *N*-(2-acetamido)-2-aminoethane sulfonic acid (ACES). For infections, bacterial overnight cultures were prepared in ACES yeast extract (AYE) medium at a starting OD_{600} of 0.1 and were grown (21 h, 37°C) until early stationary phase (2×10^9 bacteria/mL). Chloramphenicol (Cam; 5 µg/mL) was supplemented when necessary.

4.2 Cell surface and cell size analysis

All cell lines were cultivated at low density a few days before analysis ($<10^6$ cells/mL). To determine the surface of contact area between cells and culture plastic dishes, phase-contrast images were analyzed using ImageJ. To measure cell size based on electric current exclusion (CASY technology), cells were resuspended at a density of 5×10^5 cells/mL in culture medium. After 2 h shaking, 200 µL cells were added to 10 mL CASYton solution and analyzed using a CASY TTC instrument equipped with a 60 µm diameter capillary (OMNI Life Science, Germany), kindly provided by Nicolas Talarek, IGMM/CNRS Montpellier.

4.3 Plasmid construction

All plasmids are described in Table S1. Rtnlc, Sec22b, Use1, Ufe1 coding sequences were obtained by PCR from a cDNA library with the corresponding oligonucleotides (Table S2), cloned in the indicated vectors and sequenced. Plasmids kindly provided by colleagues include pCsA-SibA (P. Cosson; Centre Médical Universitaire, Geneva, Switzerland), as well as RFP-2×FYVE and GFP-2×FYVE (J. King; University of Sheffield, Sheffield, UK). Translational fusions of mRFPmars with wild-type Sey1 or the catalytically inactive mutant (Sey1_K154A) were constructed by digestion of pBS001 or pNP108, respectively, with BglII

For Peer Review

and SpeI. Subsequently, the ORFs of Sey1 or Sey1_K154A were cloned into the BglII and SpeI sites of pDM318, yielding pBS003 and pBS004, respectively.

4.4 Inactivation of *sey1* and *rtnlc*

A schematic representation of the strategies followed for genetic inactivation of *sey1* and *rtnlc*, and PCR based identification is given in Figure S7. Δ*sey1* cells (*sey1* gene ID: DDB_G0279823) were generated as follows. To construct the knockout vector (pFL1439), the 5' fragment was amplified from genomic DNA with sense (OL1135) and antisense (OL1136) oligonucleotides (from position 1 to 595 of the genomic DNA) and cloned into pBlueScript vector (Stratagene, La Jolla, CA). The 3' fragment was obtained by PCR using the GFP-Sey1 plasmid as template with sense (OL1137) and antisense (OL1138) oligonucleotides (from position 2005 to 2862 of the genomic DNA) and cloned into pBlueScript containing the 5' fragment. After sequencing, the knockout vector was completed by inserting the blasticidin resistance cassette between the two 5'and 3' fragments. The resulting plasmid was linearized (KpnI and NotI digestion) and electroporated into Ax3 cells as reported (Alibaud *et al.*, 2003). Transformants were selected in presence of 10 µg/mL blasticidin. Individual colonies were tested by PCR to confirm *sey1* gene replacement.

Δ*rtnlc* cells (*rtnlc* gene ID: DDB_G0293088) were generated as follows. To obtain the knockout vector (pFL1477), the 5' fragment was amplified from pFL1472 with sense (OL1198) and antisense (OL1199) oligonucleotides (from position 192 to 584 of the genomic DNA) and cloned into pBlueScript vector. The 3' fragment was obtained by PCR from genomic DNA using sense (OL1200) and antisense (OL1201) oligonucleotides (from position 852 to 1243 of the genomic DNA) and cloned into pBlueScript containing the 5' fragment. After sequencing, the knockout vector was completed by inserting the blasticidin resistance cassette between the two 5' and 3' fragments. Ax3 cells were electroporated with the

For Peer Review

linearized vector (KpnI and NotI digestion), and Δ*rtnlc* clones were selected as described above for Sey1.

4.5 Endocytosis, exocytosis, glycosidase and proteolytic activities

Analysis of fluid phase (Alexa-Fluor-647-dextran; Molecular Probes) uptake/exocytosis, phagocytosis of particles (YG-fluorescent 1-µm latex beads; Polysciences) or GFP-producing *K. pneumoniae* bacteria, was performed by flow cytometry as previously described (Lima *et al.*, 2012) (BD FACSCanto II, bdbiosciences). All data were normalized to protein content.

Intracellular and secreted glycosidase activities were measured as previously described (Froquet *et al.*, 2008, Le Coadic *et al.*, 2013). CtsD activity was analyzed by measuring the fluorescence release of a specific fluorogenic substrate (Mca-Gly-Lys-Pro-Ile-Leu-Phe-Phe-Arg-Leu-Lys(Dnp)-D-Arg-NH2 [Mca = (7-methoxycoumarin-4-yl)acetyl; Dnp = dinitro-phenyl]; BML-P145-0001, Enzo) with a microplate reader (Spark 20M, Tecan Life Sciences).

Lysozymes enzymatic activity in cell lysates was measured by the reduction of turbidity of heat-killed *Micrococcus lysodeikticus* (Sigma) in suspension or on agarose plates as described (Le Coadic *et al.*, 2013, Bodinier *et al.*, 2020). To measure intracellular proteolysis, 50 mg carboxylate-modified microspheres, 2.0 µm, blue fluorescent (365/415nm) (FluoSpheres, Molecular Probes, Thermofisher) were incubated overnight with 1 mg DQ-Green-labeled BSA (Invitrogen, Thermofisher) under continuous rotation. Coated beads were washed by five cycles of low speed centrifugation and resuspension in culture medium. Cells were next incubated with beads for 30 min, washed, and further incubated for 30 min. Intracellular proteolysis of BSA released DQ-Green fluorescence (505/515 nm), and intrinsic fluorescence of the beads (365/415nm) were measured by flow cytometry.

4.6 Analysis of the UPR pathway

For Peer Review

To analyze cell viability upon tunicamycin (TN) treatment, cells were seeded at 1-2 × 10^5 cells/well on 24 wells tissue culture plates and treated with TN. At the indicated times, cells were resuspended by pipetting, and propidium iodide was added for 10 min before flow cytometry analysis.

Analysis of PDI, CdcD and EHD production was performed by Western blotting as reported (Dominguez-Martin *et al.*, 2018b). Briefly, cells were first seeded at 10^6 cells/well on 6-wells tissue culture plates. After incubation for 24 h with 1.5 µg/mL TN, cells were washed once in phosphate buffer, and lysed for 30 min on ice in RIPA lysis buffer (10 mM Tris-HCl, pH 7.5, 150 mM NaCl, 0.5 mM EDTA, 0.5% NP-40, 0.05% SDS, protease inhibitors) (100µL/well). Protein concentrations were determined and adjusted before SDS polyacrylamide electrophoresis and immunoblotting were performed as previously described (Cornillon *et al.*, 2000). Proteins were revealed by ECL (Thermo Scientific, Courtaboeuf, France) and a ChemiDoc MP imager (Bio-Rad, Marnes-la-Coquette, France) allowing signal quantification (ImageQuant software).

4.7 Immunofluorescence microscopy

Antibodies used in this study are described in Table S3. Anti-p97 (CdcD) and Alexa-Fluor-647-coupled anti-p80 antibodies were kindly provided by L. Eichinger (University of Cologne, Cologne, Germany) and P. Cosson (Centre Médical Universitaire, Geneva, Switzerland), respectively. Actin was stained with TRITC-labeled phalloidin (Sigma-Aldrich). For immunofluorescence analysis of uninfected *D. discoideum*, cells were fixed and processed as previously detailed (Dias *et al.*, 2013). Cells were observed with an inverted Zeiss Axio Observer microscope or by confocal microscopy (either Leica SPE or Zeiss Confocal ZEISS 880 with Fast Airyscan).

For Peer Review

4.8 Live cell imaging and analysis

To analyze cell motility, cells were deposed on 35 mm glass bottom dish (Ibidi) in filtered HL5 medium and imaged with a spinning disc Nikon Ti Andor CSU-W1 confocal microscope every 30 s for 30 min. Films were processed by manual centroid tracking with the ImageJ plugin MTrackJ. To analyze microtubule and calnexin dynamics, cells were attached to glass coverslips in filtered HL5 medium for at least 30 min and overlaid with a 1 mm thin agarose sheet before observation. Images were taken every second for 2 min with a confocal ZEISS 880 microscope equipped with Fast Airyscan detection.

4.9 Intracellular growth and killing of *L. pneumophila* in *D. discoideum*

Intracellular replication of *L. pneumophila* JR32 and Δ*icmT* in *D. discoideum* Ax3 and Δ*sey1* mutant cells was analyzed by colony forming units (CFUs) as well as by increase in relative fluorescent units (RFUs) following intravacuolar replication of mCherry-producing *L. pneumophila* strains. To determine CFUs, GFP-producing *D. discoideum* Ax3 or Δ*sey1* amoebae were seeded at a density of 1×10^5 cells/mL in cell culture-treated 96-wells plates (VWR) and cultivated at 23°C in HL5 medium containing geneticin (G418, 20 µg/mL). Afterwards, the amoebae were infected (MOI 1) with early stationary phase *L. pneumophila* JR32 or Δ*icmT* constitutively producing mCherry, diluted in MB medium (Solomon *et al.*, 2000), centrifuged (450 *g*, 10 min, RT) and incubated for 1 h at 25°C. Subsequently, the infected amoebae were washed 3 times with MB medium and incubated at 25°C for the time indicated (96-wells plate was kept moist by addition of ddH_2O in surrounding wells). The cells were lysed with 0.8% saponin (Sigma-Aldrich) for 10 min at RT, and dilutions were plated on CYE agar plates containing Cam (5µg/mL) and incubated at 37°C for 3 days. CFUs were assessed using an automated colony counter (CounterMat Flash 4000, IUL Instruments, CounterMat software), and the number of CFUs (per mL) was calculated. Using the same

For Peer Review

procedure, killing of mCherry-producing *L. pneumophila* Δ*icmT* (MOI 50) was assessed in GFP-producing *D. discoideum* Ax3 or Δ*sey1*. Following CFU counting, the percentage of surviving bacteria (in relation to the initial bacteria number) was calculated for each time point.

To determine increase in fluorescence derived from intracellular replication of mCherry-producing *L. pneumophila*, GFP-producing *D. discoideum* Ax3 or Δ*sey1* amoebae were seeded at a density of 1×10^5 cells/mL in cell culture-treated 96-wells plates (VWR) and cultivated at 23°C in HL5 medium containing geneticin (G418, 20 µg/mL). The cells were infected (MOI 1) with early stationary phase mCherry-producing *L. pneumophila* JR32, diluted in MB medium, centrifuged (450 *g*, 10 min, RT) and incubated for 1 h at 25ºC. Afterwards, the infected amoebae were washed 3 times with fresh MB medium and incubated at 25°C for the time indicated (96-wells plate was kept moist by addition of ddH_2O in surrounding wells). Increase in mCherry fluorescence was assessed every 2 days using a microtiter plate reader (Synergy H1, Biotek).

4.10 Confocal microscopy of infected cells

Infected *D. discoideum* amoebae were fixed and imaged by confocal microscopy. In short, exponential phase *D. discoideum* Ax3 and Δ*sey1* amoebae producing calnexin-GFP and P4C-mCherry were seeded in cell culture-treated 6-wells plates (VWR) at a density of 1×10^5 cells/mL or 2×10^5 cells/mL respectively, and cultured overnight at 23ºC in HL5 medium containing geneticin (G418, 20 µg/mL) and hygromycin (50 µg/mL). The cells were infected (MOI 5) with mCerulean-producing *L. pneumophila* JR32 diluted in HL5, synchronized by centrifugation (450 *g*, 10 min, RT) and incubated at 25ºC for 1 h. Infected amoebae were then washed 3 times with fresh HL5 and incubated at 25ºC for the time indicated. Subsequently, infected cells (including supernatant) were collected from the 6-wells plate, centrifuged (500

For Peer Review

g, 5 min, RT) and fixed with 4% PFA (Electron Microscopy Sciences) for 30 min at RT. Fixed cells were then washed twice with Soerensen phosphate buffer (SorC) (Malchow *et al.*, 1972), transferred to a 8-wells µ-slide dish (Ibidi) and embedded under a layer of PBS/0.5% agarose.

The samples were imaged with a Leica TCS SP8 X CLSM (HC PL APO CS2, objective 63×/1.4–0.60 oil; Leica Microsystems) with a scanning speed of 400 Hz, bi-directional laser scan and line accumulation equal 2. Pictures were acquired with a pinhole of 1.19 Airy Units (AU) and with a pixel/voxel size close to the instrument's Nyquist criterion of 43×43×130 nm (xyz). Images were deconvolved with Huygens professional version 19.10 software (Scientific Volume Imaging, http://svi.nl) using the CMLE algorithm, set to 40 iterations and quality threshold of 0.05. Z-stacks were finalized/exported using Imaris 9.5.0 software (Bitplane).

4.11 Imaging flow cytometry

Processing of infected amoebae for imaging flow cytometry (IFC) was performed essentially as described (Welin *et al.*, 2018). In short, *D. discoideum* Ax3 and Δ*sey1* mutant producing calnexin-GFP and P4C-mCherry were seeded in T-75 flasks containing HL5 medium, geneticin (G418, 20 µg/mL) and hygromycin (50 µg/mL), and infected (MOI 5) with mPlum-producing *L. pneumophila* JR32 diluted in HL5 medium. The infection was synchronized by centrifugation (450 *g*, 10 min, RT), and the cells were incubated for 1 h at 25ºC. Infected cells were then washed three times with HL5 and incubated at 25ºC for the time indicated. Afterwards, cells were collected, centrifuged (500 *g*, 5 min, RT) and fixed in 2% PFA for 90 min on ice. Fixed infected amoebae were washed twice in phosphate-buffered saline (PBS) and resuspended in 20 µL ice-cold PBS prior to IFC analysis.

For Peer Review

Using an imaging flow cytometer (ImageStreamX MkII; Amnis), at least 5'000 cells were acquired and analyzed with the IDEAS (v.6.2) software (Amnis). In short, infected amoebae containing one intracellular *L. pneumophila* bacterium were gated and analyzed for colocalization of GFP and mCherry (host) with mPlum produced by *L. pneumophila* (minimum number of gated events specified in the figure legend). The software computes the IFC colocalization score (bright detail similarity), which is the log-transformed Pearson's correlation coefficient of the localized bright spots with a radius of 3 pixels or less in two images, and is used to quantify relative enrichment of a marker on the LCV. Data analysis was performed using GraphPad Prism. Regular two-way ANOVA followed by Bonferroni post-hoc test was used to compare all samples between each other.

4.12 Electron microscopy

L. pneumophila-infected *D. discoideum* Ax3, Δ*sey1* producing GFP or Δ*sey1* producing GFP-Sey1 were fixed with 4% PFA and 0.1% glutaraldehyde in 0.1 M sodium cacodylate buffer (pH 7.35) for 30 min at 4ºC. Afterwards, the samples were treated sequentially with 2.5% glutaraldehyde for 30 min, 1% OsO_4 for 1 h at 0°C, both in 0.1 M sodium cacodylate buffer and 2% uranyl acetate in ddH_2O for 1 h at 4°C, followed by embedment in 2% Difco Noble agar (BD Biosciences, Allschwil, Switzerland) in H_2O to form an immobilized pellet. An increasing ethanol series (50%-100%) was then used to dehydrate the samples, which were finally embedded in Epon/Araldite (Sigma-Aldrich). Contrast enhancement of ultrathin (50 nm) sections was done using Reynolds lead citrate. Processed samples were examined with a CM100 transmission electron microscope (Thermo Fisher Scientific, Eindhoven, The Netherlands) at an acceleration voltage of 80 kV using an Orius 1000 digital camera (Ametek GmbH, Munich, Germany).

For Peer Review

ACKNOWLEDGEMENTS

Confocal laser scanning microscopy and TEM was performed using equipment of the Center of Microscopy and Image Analysis, University of Zurich (UZH), run by Andres Kaech and Urs Ziegler. Imaging Flow Cytometry was performed at the Flow Cytometry Core Facility of the Faculty of Medicine and Health Sciences, Linköping University, Linköping, Sweden. Flow cytometry and microscopy analyses of uninfected cells were performed at the Montpellier RIO imaging facility of the University of Montpellier, member of the national infrastructure France-BioImaging, supported by the French National Research Agency (ANR-10-INBS-04, "Investments for the future"). Work in the group of H.H. was supported by the Swiss National Science Foundation (SNF; 31003A_175557), the Novartis Foundation for Medical-Biological Research, and the OPO foundation. Work in the group of V.M. and F.L. was supported by the Région Occitanie. A.W. was supported by grants from the Swedish Society of Medicine (SLS-934829) and the Åke Wiberg Foundation. The funders had no role in study design, data collection and analysis, decision to publish, or preparation of the manuscript.

AUTHORS' CONTRIBUTION

H.H. and F.L. conceived the study and guided experiments. D.H., Be.S., A.W., Bi.S., A.L.S. and F.L. designed and conducted experiments. V.M. provided funding. H.H. and F.L. wrote the paper with input from all other authors.

CONFLIT OF INTEREST

The authors declare no conflict of interest.

For Peer Review

REFERENCES

Al-Quadan, T., Price, C.T. and Abu Kwaik, Y. (2012). Exploitation of evolutionarily conserved amoeba and mammalian processes by *Legionella*. *Trends in Microbiology* **20,** 299-306.

Alibaud, L., Cosson, P. and Benghezal, M. (2003). *Dictyostelium discoideum* transformation by oscillating electric field electroporation. *BioTechniques* **35,** 78-80, 82-73.

Alibaud, L., Kohler, T., Coudray, A., Prigent-Combaret, C., Bergeret, E., Perrin, J., *et al.* (2008). *Pseudomonas aeruginosa* virulence genes identified in a *Dictyostelium* host model. *Cellular Microbiology* **10,** 729-740.

Almanza, A., Carlesso, A., Chintha, C., Creedican, S., Doultsinos, D., Leuzzi, B., *et al.* (2019). Endoplasmic reticulum stress signalling - from basic mechanisms to clinical applications. *The FEBS Journal* **286,** 241-278.

Anwar, K., Klemm, R.W., Condon, A., Severin, K.N., Zhang, M., Ghirlando, R., *et al.* (2012). The dynamin-like GTPase Sey1p mediates homotypic ER fusion in *S. cerevisiae*. *The Journal of Cell Biology* **197,** 209-217.

Asrat, S., de Jesus, D.A., Hempstead, A.D., Ramabhadran, V. and Isberg, R.R. (2014). Bacterial pathogen manipulation of host membrane trafficking. *Annual Review of Cell and Developmental Biology* **30,** 79-109.

Bärlocher, K., Welin, A. and Hilbi, H. (2017). Formation of the *Legionella* replicative compartment at the crossroads of retrograde trafficking. *Frontiers in Cellular and Infection Microbiology* **7,** 482.

Bian, X., Klemm, R.W., Liu, T.Y., Zhang, M., Sun, S., Sui, X., *et al.* (2011). Structures of the atlastin GTPase provide insight into homotypic fusion of endoplasmic reticulum membranes. *Proceedings of the National Academy of Sciences of the United States of America* **108,** 3976-3981.

For Peer Review

Bodinier, R., Leiba, J., Sabra, A., Jauslin, T.N., Lamrabet, O., Guilhen, C., *et al.* (2020). LrrkA, a kinase with leucine-rich repeats, links folate sensing with Kil2 activity and intracellular killing. *Cellular Microbiology* **22,** e13129.

Byrnes, L.J., Singh, A., Szeto, K., Benvin, N.M., O'Donnell, J.P., Zipfel, W.R. and Sondermann, H. (2013). Structural basis for conformational switching and GTP loading of the large G protein atlastin. *The EMBO Journal* **32,** 369-384.

Byrnes, L.J. and Sondermann, H. (2011). Structural basis for the nucleotide-dependent dimerization of the large G protein atlastin-1/SPG3A. *Proceedings of the National Academy of Sciences of the United States of America* **108,** 2216-2221.

Cao, P., Renna, L., Stefano, G. and Brandizzi, F. (2016). SYP73 Anchors the ER to the actin cytoskeleton for maintenance of ER integrity and streaming in *Arabidopsis*. *Current Biology* **26,** 3245-3254.

Cardenal-Munoz, E., Barisch, C., Lefrancois, L.H., Lopez-Jimenez, A.T. and Soldati, T. (2017). When Dicty met Myco, a (not so) romantic story about one amoeba and its intracellular pathogen. *Frontiers in Cellular and Infection Microbiology* **7,** 529.

Carnell, M., Zech, T., Calaminus, S.D., Ura, S., Hagedorn, M., Johnston, S.A., *et al.* (2011). Actin polymerization driven by WASH causes V-ATPase retrieval and vesicle neutralization before exocytosis. *The Journal of Cell Biology* **193,** 831-839.

Charette, S.J. and Cosson, P. (2007). A LYST/beige homolog is involved in biogenesis of *Dictyostelium* secretory lysosomes. *Journal of Cell Science* **120,** 2338-2343.

Charette, S.J. and Cosson, P. (2008). Altered composition and secretion of lysosome-derived compartments in *Dictyostelium* AP-3 mutant cells. *Traffic* **9,** 588-596.

Chen, J., Stefano, G., Brandizzi, F. and Zheng, H. (2011). Arabidopsis RHD3 mediates the generation of the tubular ER network and is required for Golgi distribution and motility in plant cells. *Journal of Cell Science* **124,** 2241-2252.

For Peer Review

Chen, Q., Xiao, Y., Chai, P., Zheng, P., Teng, J. and Chen, J. (2019). ATL3 is a tubular ER-phagy receptor for GABARAP-mediated selective autophagy. *Current Biology* **29,** 846-855.

Cornillon, S., Pech, E., Benghezal, M., Ravanel, K., Gaynor, E., Letourneur, F., *et al.* (2000). Phg1p is a nine-transmembrane protein superfamily member involved in *Dictyostelium* adhesion and phagocytosis. *The Journal of Biological Chemistry* **275,** 34287-34292.

Dias, M., Blanc, C., Thazar-Poulot, N., Ben Larbi, S., Cosson, P. and Letourneur, F. (2013). *Dictyostelium* ACAP-A is an ArfGAP involved in cytokinesis, cell migration and actin cytoskeleton dynamics. *Journal of Cell Science* **126,** 756-766.

Dominguez-Martin, E., Hernandez-Elvira, M., Vincent, O., Coria, R. and Escalante, R. (2018a). Unfolding the endoplasmic reticulum of a social amoeba: *Dictyostelium discoideum* as a new model for the study of endoplasmic reticulum stress. *Cells* **7,** 56.

Dominguez-Martin, E., Ongay-Larios, L., Kawasaki, L., Vincent, O., Coello, G., Coria, R. and Escalante, R. (2018b). IreA controls endoplasmic reticulum stress-induced autophagy and survival through homeostasis recovery. *Molecular and Cellular Biology* **38,** e00054-18.

Draberova, E., Vinopal, S., Morfini, G., Liu, P.S., Sladkova, V., Sulimenko, T., *et al.* (2011). Microtubule-severing ATPase spastin in glioblastoma: increased expression in human glioblastoma cell lines and inverse roles in cell motility and proliferation. *The Journal of Neuropathology and Experimental Neurology* **70,** 811-826.

English, A.R., Zurek, N. and Voeltz, G.K. (2009). Peripheral ER structure and function. *Current Opinion in Cell Biology* **21,** 596-602.

Escoll, P., Song, O.R., Viana, F., Steiner, B., Lagache, T., Olivo-Marin, J.C., *et al.* (2017). *Legionella pneumophila* modulates mitochondrial dynamics to trigger metabolic repurposing of infected macrophages. *Cell Host & Microbe* **22,** 302-316.

For Peer Review

Espadas, J., Pendin, D., Bocanegra, R., Escalada, A., Misticoni, G., Trevisan, T., *et al.* (2019). Dynamic constriction and fission of endoplasmic reticulum membranes by reticulon. *Nat Commun* **10,** 5327.

Evans, K., Keller, C., Pavur, K., Glasgow, K., Conn, B. and Lauring, B. (2006). Interaction of two hereditary spastic paraplegia gene products, spastin and atlastin, suggests a common pathway for axonal maintenance. *Proceedings of the National Academy of Sciences of the United States of America* **103,** 10666-10671.

Fink, J.K. (2013). Hereditary spastic paraplegia: clinico-pathologic features and emerging molecular mechanisms. *Acta Neuropathol*ogy **126,** 307-328.

Finsel, I. and Hilbi, H. (2015). Formation of a pathogen vacuole according to *Legionella pneumophila*: how to kill one bird with many stones. *Cellular Microbiology* **17,** 935-950.

Fischer, D., Schabhuttl, M., Wieland, T., Windhager, R., Strom, T.M. and Auer-Grumbach, M. (2014). A novel missense mutation confirms ATL3 as a gene for hereditary sensory neuropathy type 1. *Brain* **137,** e286.

Froquet, R., Cherix, N., Birke, R., Benghezal, M., Cameroni, E., Letourneur, F., *et al.* (2008). Control of cellular physiology by TM9 proteins in yeast and *Dictyostelium*. *The Journal of Biological Chemistry* **283,** 6764-6772.

Froquet, R., le Coadic, M., Perrin, J., Cherix, N., Cornillon, S. and Cosson, P. (2012). TM9/Phg1 and SadA proteins control surface expression and stability of SibA adhesion molecules in *Dictyostelium*. *Molecular Biology of the Cell* **23,** 679-686.

Gomez-Valero, L., Rusniok, C., Cazalet, C. and Buchrieser, C. (2011). Comparative and functional genomics of *Legionella* identified eukaryotic like proteins as key players in host-pathogen interactions. *Frontiers in Microbiology* **2,** 208.

For Peer Review

Grigoriev, I., Gouveia, S.M., van der Vaart, B., Demmers, J., Smyth, J.T., Honnappa, S., *et al.* (2008). STIM1 is a MT-plus-end-tracking protein involved in remodeling of the ER. *Current Biology* **18,** 177-182.

Guelly, C., Zhu, P.P., Leonardis, L., Papic, L., Zidar, J., Schabhuttl, M., *et al.* (2011). Targeted high-throughput sequencing identifies mutations in atlastin-1 as a cause of hereditary sensory neuropathy type I. *American Journal of Human Genetics* **88,** 99-105.

Hoffmann, C., Finsel, I., Otto, A., Pfaffinger, G., Rothmeier, E., Hecker, M., *et al.* (2014). Functional analysis of novel Rab GTPases identified in the proteome of purified *Legionella*-containing vacuoles from macrophages. *Cellular Microbiology* **16,** 1034-1052.

Hu, J., Shibata, Y., Zhu, P.P., Voss, C., Rismanchi, N., Prinz, W.A., *et al.* (2009). A class of dynamin-like GTPases involved in the generation of the tubular ER network. *Cell* **138,** 549-561.

Isberg, R.R., O'Connor, T.J. and Heidtman, M. (2009). The *Legionella pneumophila* replication vacuole: making a cosy niche inside host cells. *Nature Reviews Microbiology* **7,** 13-24.

Journet, A., Chapel, A., Jehan, S., Adessi, C., Freeze, H., Klein, G. and Garin, J. (1999). Characterization of *Dictyostelium discoideum* cathepsin D. *Journal of Cell Science* **112,** 3833-3843.

Jozsef, L., Tashiro, K., Kuo, A., Park, E.J., Skoura, A., Albinsson, S., *et al.* (2014). Reticulon 4 is necessary for endoplasmic reticulum tubulation, STIM1-Orai1 coupling, and store-operated calcium entry. *The Journal of Biological Chemistry* **289,** 9380-9395.

Kagan, J.C. and Roy, C.R. (2002). *Legionella* phagosomes intercept vesicular traffic from endoplasmic reticulum exit sites. *Nature Cell Biology* **4,** 945-954.

For Peer Review

Kagan, J.C., Stein, M.P., Pypaert, M. and Roy, C.R. (2004). *Legionella* subvert the functions of Rab1 and Sec22b to create a replicative organelle. *The Journal of Experimental Medicine* **199,** 1201-1211.

Kim, K.T., Moon, Y., Jang, Y., Lee, K.T., Lee, C., Jun, Y. and Lee, S. (2017). Molecular mechanisms of atlastin-mediated ER membrane fusion revealed by a FRET-based single-vesicle fusion assay. *Scientific Reports* **7,** 8700.

Klemm, R.W., Norton, J.P., Cole, R.A., Li, C.S., Park, S.H., Crane, M.M., *et al.* (2013). A conserved role for atlastin GTPases in regulating lipid droplet size. *Cell Reports* **3,** 1465-1475.

Klopfenstein, D.R., Kappeler, F. and Hauri, H.P. (1998). A novel direct interaction of endoplasmic reticulum with microtubules. *The EMBO Journal* **17,** 6168-6177.

Krols, M., Detry, S., Asselbergh, B., Almeida-Souza, L., Kremer, A., Lippens, S., *et al.* (2018). Sensory-neuropathy-causing mutations in ATL3 cause aberrant ER membrane tethering. *Cell Reports* **23,** 2026-2038.

Lai, Y.S., Stefano, G. and Brandizzi, F. (2014). ER stress signaling requires RHD3, a functionally conserved ER-shaping GTPase. *Journal of Cell Science* **127,** 3227-3232.

Lamrabet, O., Jauslin, T., Lima, W.C., Leippe, M. and Cosson, P. (2020). The multifarious lysozyme arsenal of *Dictyostelium discoideum*. *Developmental and Comparative Immunology* **107,** 103645.

Le Coadic, M., Froquet, R., Lima, W.C., Dias, M., Marchetti, A. and Cosson, P. (2013). Phg1/TM9 proteins control intracellular killing of bacteria by determining cellular levels of the Kil1 sulfotransferase in *Dictyostelium*. *PloS One* **8,** e53259.

Lee, M., Paik, S.K., Lee, M.J., Kim, Y.J., Kim, S., Nahm, M., *et al.* (2009). *Drosophila* atlastin regulates the stability of muscle microtubules and is required for synapse development. *Developmental Biology* **330,** 250-262.

For Peer Review

Liang, J.R., Lingeman, E., Ahmed, S. and Corn, J.E. (2018). Atlastins remodel the endoplasmic reticulum for selective autophagy. *The Journal of Cell Biology* **217,** 3354-3367.

Lima, W.C., Leuba, F., Soldati, T. and Cosson, P. (2012). Mucolipin controls lysosome exocytosis in *Dictyostelium*. *Journal of Cell Science* **125,** 2315-2322.

Liu, T.Y., Bian, X., Romano, F.B., Shemesh, T., Rapoport, T.A. and Hu, J. (2015). Cis and trans interactions between atlastin molecules during membrane fusion. *Proceedings of the National Academy of Sciences of the United States of America* **112,** E1851-1860.

Liu, T.Y., Bian, X., Sun, S., Hu, X., Klemm, R.W., Prinz, W.A., *et al.* (2012). Lipid interaction of the C terminus and association of the transmembrane segments facilitate atlastin-mediated homotypic endoplasmic reticulum fusion. *Proceedings of the National Academy of Sciences of the United States of America* **109,** E2146-2154.

Malchow, D., Nagele, B., Schwarz, H. and Gerisch, G. (1972). Membrane-bound cyclic AMP phosphodiesterase in chemotactically responding cells of *Dictyostelium discoideum*. *European Journal of Biochemistry / FEBS* **28,** 136-142.

Niu, L., Ma, T., Yang, F., Yan, B., Tang, X., Yin, H., *et al.* (2019). Atlastin-mediated membrane tethering is critical for cargo mobility and exit from the endoplasmic reticulum. *Proceedings of the National Academy of Sciences of the United States of America* **116,** 14029-14038.

O'Donnell, J.P., Byrnes, L.J., Cooley, R.B. and Sondermann, H. (2018). A hereditary spastic paraplegia-associated atlastin variant exhibits defective allosteric coupling in the catalytic core. *The Journal of Biological Chemistry* **293,** 687-700.

Ogawa-Goto, K., Tanaka, K., Ueno, T., Tanaka, K., Kurata, T., Sata, T. and Irie, S. (2007). p180 is involved in the interaction between the endoplasmic reticulum and microtubules

For Peer Review

through a novel microtubule-binding and bundling domain. *Molecular Biology of the Cell* **18,** 3741-3751.

Orso, G., Pendin, D., Liu, S., Tosetto, J., Moss, T.J., Faust, J.E., *et al.* (2009). Homotypic fusion of ER membranes requires the dynamin-like GTPase atlastin. *Nature* **460,** 978-983.

Park, S.H., Zhu, P.P., Parker, R.L. and Blackstone, C. (2010). Hereditary spastic paraplegia proteins REEP1, spastin, and atlastin-1 coordinate microtubule interactions with the tubular ER network. *The Journal of Clinical Investigation* **120,** 1097-1110.

Pawar, S., Ungricht, R., Tiefenboeck, P., Leroux, J.C. and Kutay, U. (2017). Efficient protein targeting to the inner nuclear membrane requires atlastin-dependent maintenance of ER topology. *eLife* **6,** e28202.

Personnic, N., Bärlocher, K., Finsel, I. and Hilbi, H. (2016). Subversion of retrograde trafficking by translocated pathogen effectors. *Trends in Microbiology* **24,** 450-462.

Phillips, M.J. and Voeltz, G.K. (2016). Structure and function of ER membrane contact sites with other organelles. *Nature Reviews Molecular and Cell Biology* **17,** 69-82.

Rismanchi, N., Soderblom, C., Stadler, J., Zhu, P.P. and Blackstone, C. (2008). Atlastin GTPases are required for Golgi apparatus and ER morphogenesis. *Human molecular genetics* **17,** 1591-1604.

Robinson, C.G. and Roy, C.R. (2006). Attachment and fusion of endoplasmic reticulum with vacuoles containing *Legionella pneumophila*. *Cellular Microbiology* **8,** 793-805.

Rogers, J.V., McMahon, C., Baryshnikova, A., Hughson, F.M. and Rose, M.D. (2014). ER-associated retrograde SNAREs and the Dsl1 complex mediate an alternative, Sey1p-independent homotypic ER fusion pathway. *Molecular Biology of the Cell* **25,** 3401-3412.

Rothmeier, E., Pfaffinger, G., Hoffmann, C., Harrison, C.F., Grabmayr, H., Repnik, U., *et al.* (2013). Activation of Ran GTPase by a *Legionella* effector promotes microtubule polymerization, pathogen vacuole motility and infection. *PLoS Pathogens* **9,** e1003598.

For Peer Review

Salinas, S., Proukakis, C., Crosby, A. and Warner, T.T. (2008). Hereditary spastic paraplegia: clinical features and pathogenetic mechanisms. *Lancet Neurology* **7,** 1127-1138.

Sanderson, C.M., Connell, J.W., Edwards, T.L., Bright, N.A., Duley, S., Thompson, A., *et al.* (2006). Spastin and atlastin, two proteins mutated in autosomal-dominant hereditary spastic paraplegia, are binding partners. *Human molecular genetics* **15,** 307-318.

Schwarz, D.S. and Blower, M.D. (2016). The endoplasmic reticulum: structure, function and response to cellular signaling. *Cellular and Molecular Life Sciences* **73,** 79-94.

Sherwood, R.K. and Roy, C.R. (2016). Autophagy evasion and endoplasmic reticulum subversion: the Yin and Yang of *Legionella* intracellular infection. *Annual Reviews in Microbiology* **70,** 413-433.

Shibata, Y., Hu, J., Kozlov, M.M. and Rapoport, T.A. (2009). Mechanisms shaping the membranes of cellular organelles. *Annual Reviews of Cell and Developmental Biology* **25,** 329-354.

Shibata, Y., Voeltz, G.K. and Rapoport, T.A. (2006). Rough sheets and smooth tubules. *Cell* **126,** 435-439.

Smith, M. and Wilkinson, S. (2017). ER homeostasis and autophagy. *Essays in Biochemistry* **61,** 625-635.

Solomon, J.M. and Isberg, R.R. (2000). Growth of *Legionella pneumophila* in *Dictyostelium discoideum*: a novel system for genetic analysis of host-pathogen interactions. *Trends in Microbiology* **8,** 478-480.

Song, S., Tan, J., Miao, Y. and Zhang, Q. (2018). Crosstalk of ER stress-mediated autophagy and ER-phagy: Involvement of UPR and the core autophagy machinery. *Journal of Cell Physiology* **233,** 3867-3874.

Stefano, G., Renna, L. and Brandizzi, F. (2014). The endoplasmic reticulum exerts control over organelle streaming during cell expansion. *Journal of Cell Science* **127,** 947-953.

For Peer Review

Stefano, G., Renna, L., Lai, Y., Slabaugh, E., Mannino, N., Buono, R.A., *et al.* (2015). ER network homeostasis is critical for plant endosome streaming and endocytosis. *Cell Discovery* **1,** 15033.

Steiner, B., Swart, A.L., Welin, A., Weber, S., Personnic, N., Kaech, A., *et al.* (2017). ER remodeling by the large GTPase atlastin promotes vacuolar growth of *Legionella pneumophila*. *EMBO Reports* **18,** 1817-1836.

Steiner, B., Weber, S. and Hilbi, H. (2018a). Formation of the *Legionella*-containing vacuole: phosphoinositide conversion, GTPase modulation and ER dynamics. *International Journal of Medical Microbiology* **308,** 49-57.

Steiner, B., Weber, S., Kaech, A., Ziegler, U. and Hilbi, H. (2018b). The large GTPase atlastin controls ER remodeling around a pathogen vacuole. *Communicative & Integrative Biology* **11,** 1-5.

Stolz, A. and Grumati, P. (2019). The various shades of ER-phagy. *The FEBS Journal* **286,** 4642-4649.

Swanson, M.S. and Isberg, R.R. (1995). Association of *Legionella pneumophila* with the macrophage endoplasmic reticulum. *Infection and Immunity* **63,** 3609-3620.

Swart, A.L., Harrison, C.F., Eichinger, L., Steinert, M. and Hilbi, H. (2018). *Acanthamoeba* and *Dictyostelium* as cellular models for *Legionella* infection. *Frontiers in Cellular and Infection Microbiology* **8,** 61.

Swart, A.L. and Hilbi, H. (2020a). Phosphoinositides and the fate of *Legionella* in phagocytes. *Frontiers in Immunology* **11,** 25.

Swart, A.L., Steiner, B., Gomez-Valero, L., Schutz, S., Hannemann, M., Janning, P., *et al.* (2020b). Divergent evolution of *Legionella* RCC1 repeat effectors defines the range of Ran GTPase cycle targets. *mBio* **11,** e00405-20.

For Peer Review

Voeltz, G.K., Prinz, W.A., Shibata, Y., Rist, J.M. and Rapoport, T.A. (2006). A class of membrane proteins shaping the tubular endoplasmic reticulum. *Cell* **124,** 573-586.

Voss, C., Lahiri, S., Young, B.P., Loewen, C.J. and Prinz, W.A. (2012). ER-shaping proteins facilitate lipid exchange between the ER and mitochondria in *S. cerevisiae*. *Journal of Cell Science* **125,** 4791-4799.

Wang, S., Tukachinsky, H., Romano, F.B. and Rapoport, T.A. (2016). Cooperation of the ER-shaping proteins atlastin, lunapark, and reticulons to generate a tubular membrane network. *eLife* **5,** e18605.

Weber, S. and Hilbi, H. (2014a). Live cell imaging of phosphoinositide dynamics during *Legionella* infection. *Methods in Molecular Biology* **1197,** 153-167.

Weber, S., Steiner, B., Welin, A. and Hilbi, H. (2018). *Legionella*-containing vacuoles capture PtdIns(4)*P*-rich vesicles derived from the Golgi apparatus. *mBio* **9,** e02420-18.

Weber, S., Wagner, M. and Hilbi, H. (2014b). Live-cell imaging of phosphoinositide dynamics and membrane architecture during *Legionella* infection. *mBio* **5,** e00839-13.

Welin, A., Weber, S. and Hilbi, H. (2018). Quantitative imaging flow cytometry of *Legionella*-infected *Dictyostelium* amoebae reveals the impact of retrograde trafficking on pathogen vacuole composition. *Applied and Environmental Microbiology* **84,** e00158-18.

Wilkinson, S. (2019). ER-phagy: shaping up and destressing the endoplasmic reticulum. *The FEBS Journal* **286,** 2645-2663.

Wilkinson, S. (2020). Emerging principles of selective ER autophagy. *Journal of Molecular Biology* **432,** 185-205.

Zhang, D., Vjestica, A. and Oliferenko, S. (2010). The cortical ER network limits the permissive zone for actomyosin ring assembly. *Current Biology* **20,** 1029-1034.

Zhang, M., Wu, F., Shi, J., Zhu, Y., Zhu, Z., Gong, Q. and Hu, J. (2013). ROOT HAIR DEFECTIVE3 family of dynamin-like GTPases mediates homotypic endoplasmic

For Peer Review

reticulum fusion and is essential for *Arabidopsis* development. *Plant Physiology* **163,** 713-720.

Zhao, G., Zhu, P.P., Renvoise, B., Maldonado-Baez, L., Park, S.H. and Blackstone, C. (2016). Mammalian knock out cells reveal prominent roles for atlastin GTPases in ER network morphology. *Experimental Cell Research* **349,** 32-44.

Zhu, Y., Zhang, G., Lin, S., Shi, J., Zhang, H. and Hu, J. (2018). Sec61beta facilitates the maintenance of endoplasmic reticulum homeostasis by associating microtubules. *Protein & Cell* **9,** 616-628.

For Peer Review

FIGURE LEGENDS

FIGURE 1 Genomic deletion of *D. discoideum sey1* and basic mutant characterization.

(**a**) Schematic representation of the strategy used to inactivate the *D. discoideum sey1* gene by insertion of the blasticidin resistance-encoding gene (BsR) by double recombination. Sey1 comprises a large guanosine triphosphatase (GTPase) domain followed by a three-helix bundle (3HB) and two adjacent transmembrane motifs (TMs). In Δ*sey1* cells, the protein sequence from amino acid residues P149 to K588 is deleted. (**b**) Phase contrast microscopy and (**c**) histogram of cell-contact area of live cells on tissue culture dishes determined after binarization of images (ImageJ) (n=100) revealed that Δ*sey1* cells are enlarged compared to parental cells (Ax3). Scale bar, 10 µm. (**d**) Representative distribution of cell diameters measured by electric current exclusion (CASY technology). Compared to Ax3 cells, Δ*sey1* cells show a greater diameter heterogeneity with a mean diameter of 10.24 ± 0.15 µm instead of 9.51 ± 0.24 µm in Ax3 cells (data represent the average and s.e.m. of four independent experiments) (**e**) Histogram showing the distribution of nuclei/cell for the indicated *D. discoideum* strains (Ax3, Δ*sey1*). Cells were stained with DAPI (4',6-diamidino-2-phenylindole; blue). 32.7% of Δ*sey1* cells showed two or more nuclei in contrast to 10.2% for Ax3 cells (n=100 cells). (**f**) Growth curves of *D. discoideum* strains cultivated in Petri-dishes plotted as a function of time (in hours, h). Compared to Ax3 cells, Δ*sey1* cells show a reduced growth rate. Doubling times are indicated (data represent the average and s.e.m. of three independent experiments). (**g**) Aggregation and development of Ax3 and Δ*sey1* cells plated on solid starvation plates and incubated at 22°C. Cellular aggregates were observed after 6 h and fruiting bodies after 24 h for both cell lines. Scale bar, 0.5 mm

FIGURE 2 *D. discoideum* Δ*sey1* shows aberrant ER morphology and dynamics.

For Peer Review

(**a**) ER morphology in Ax3 and Δ*sey1* cells analyzed by confocal microscopy after immunolabeling of the ER-resident enzyme protein disulfide isomerase (PDI). Compared to the Ax3 parental strain, Δ*sey1* cells showed clumps of PDI-positive membranous structures at the cell periphery and a few interconnected ER tubules (red arrowheads). Nuclei were stained with DAPI (in blue). Scale bars, 5 µm. (**b**) Representative confocal fluorescence micrographs of dually labeled *D. discoideum* Ax3 or Δ*sey1* mutant cells producing the ER marker calnexin A-GFP (CnxA-GFP) and the PtdIns(4)*P*-binding probe P4C-mCherry. Arrowheads, clumped peripheral ER. Scale bars, 3 µm. (**c**) Snapshots of time-lapse video microscopy analysis of amoebae producing calnexin A-GFP. The ER nodular clumps observed in Δ*sey1* cells appear mostly static (white arrowheads) in contrast to the vivid dynamics of ER tubules in mutant and parental *D. discoideum* strains (red arrowheads). N, nucleus. Scale bars, 5 µm. (**d**) Electron micrographs of Ax3 and Δ*sey1* cells. N, nucleus; arrowheads, rough ER. Scale bars, 1 µm.

FIGURE 3 Analysis of endocytic functions and growth on bacteria of Δ*sey1* cells.

(**a**) Fluid-phase uptake of dextran coupled to Alexa-Fluor-647 was measured by flow cytometry and expressed as the percentage of the maximal uptake in Ax3 cells. (**b**) Exocytosis was analyzed in cells preincubated for 4 h with Alexa-Fluor-647-dextran to fully load all endocytic compartments. After incubation in dextran-free medium for different periods of time, retained intracellular fluorescence was measured by flow cytometry and expressed as the percentage of the initial fluorescence. (**c**) Representative images of the growth of cells on lawns of *K. pneumoniae* observed after 5 days (n>3). Δ*sey1* cells were unable to grow on these bacterial lawns, whereas the production of GFP-Sey1 partially complemented this defect. (**d**) Schematic representation of cell capacities to grow on different bacterial lawns. Δ*sey1* cells showed total growth inhibition on lawns of Gram-negative *K. pneumoniae* (*K.*

For Peer Review

pneum.) and *E. coli* B/r and severely reduced growth rates on lawns of Gram-positive *B. subtilis* and *M. luteus*. Cell growth on several bacterial species was assessed as shown in (c) in three independent experiments and scored from 4 (efficient growth in all tested cell numbers) to 0 (no growth). Colored squares indicate the average score (green 4, yellow 3, orange 2, and red 0-1). (**e**) Uptake of *K. pneumoniae* was measured by flow cytometry after incubation of cells with GFP-producing bacteria for 20 min. Results are expressed as the percentage of uptake in Ax3 cells. (**f**) Phagocytic rates of Ax3 and Δ*sey1* cells incubated with fluorescent beads. Cells were incubated with 1 µm YG-labeled beads, and at the indicated time points, the internal fluorescence was measured by flow cytometry and expressed as the percent of maximal uptake by Ax3 cells. (**g**) Killing of internalized bacteria was measured upon incubation of Ax3 or Δ*sey1* cells with *K. pneumoniae.* At the indicated time points, samples were treated with Triton X-100 to selectively lyse amoebae and plated on LB-agar plates. Bacterial clones were counted after overnight incubation at 37°C. Data are expressed as the percent of surviving bacteria. All data in this figure are normalized to protein content in cells and represent the mean and s.e.m. of three independent experiments (not significant, ns: $P > 0.05$, $^{**}P < 0.01$).

FIGURE 4 Hypersecretion of lysosomal enzymes by Δ*sey1* cells.

(**a**) The enzymatic activity of lysozymes in cell lysates was measured by the reduction of turbidity of heat-killed *Micrococcus lysodeikticus* in suspension. Results are expressed as the percentage of activity of strain Ax3 (left panel). When bacteria are included in agarose gels, halos around diluted cell lysate deposits form proportionally to the extent of bacterial lysis (right panel) providing a visual estimate of enzymatic activities. (**b**) α-mannosidase and cathepsin D (CtsD) enzymatic activities were measured in cellular pellets (internal pool) and extracellular medium (secreted pool) after incubation of the Ax3 and Δ*sey1* strains indicated

For Peer Review

in culture medium for 24 h. Results are expressed as the percentage of secreted activities relatively to total internal and secreted activities. (**c**) Cathepsin D production by the Ax3 and Δ*sey1* strains indicated. Representative samples of cathepsin D (CtsD, 44 kDa) protein quantity determined by Western blot of whole cell lysates with an anti-CtsD antibody. Immunoblotting with an anti-PDI antibody was carried out to control protein amounts of loaded material. (**d**) Histogram showing calculated ratio between CtsD and PDI signals in Western blots quantified using the Image lab analysis software. Results are normalized to the CtsD/PDI ratio in Ax3 cells. (**e**) Intracellular proteolysis was measured by feeding cells with DQ Green-BSA coated beads and measuring unquenching of the fluorophore after incubation for 1 h. Proteolysis in Δ*sey1* cells is expressed as the percentage of Ax3 activity. All data presented in this figure are the mean and s.e.m. of three independent experiments (not significant, ns: $P > 0.05$, *$P < 0.05$, **$P < 0.01$, ****$P < 0.0001$).

FIGURE 5 *D. discoideum* Δ*sey1* is impaired for cell motility.

(**a**) Time-lapse video confocal microscopy of cell motility using single cell tracking analysis. The indicated Ax3 or Δ*sey1* strains were incubated in HL5 medium and imaged by spinning disk confocal microscopy. Randomly moving cells were imaged every 30 s for 30 min. Tracks of 15 randomly sampled cells are shown centered at the origin. The motility defect of Δ*sey1* cells was restored upon ectopic production of GFP-Sey1 but not of the catalytically inactive Sey1_K154A mutant. (**b**) Quantification of the maximum distance from the origin of individual cells of each cell line. The median is indicated by a line in each box extending from the upper and lower quartiles (not significant, ns: $P > 0.05$, ***$P < 0.001$).

FIGURE 6 Analysis of the UPR pathway in *D. discoideum* Δ*sey1*.

For Peer Review

(**a**) Histogram of cell viability after addition of 1.5 µg/mL tunicamycin (TN) for the indicated period of times. Viability was measured by flow cytometry analysis as exclusion of propidium iodide. Results are the mean and s.e.m. of three independent experiments (not significant, ns: $P > 0.05$, $^{**}P < 0.01$, $^{***}P < 0.001$). (**b**) The indicated cell lines were incubated with 1.5 µg/mL tunicamycin (TN) and observed by phase contrast microscopy after 48 h of incubation. Dead cells are indicated by red arrows. Scale bars, 10 µm. (**c**) Effect of the TN concentration on cell viability after 48 h of incubation. Cell viability was determined as above. (**d**) Representative Western blot analysis of CdcD and PDI protein production in cells after addition of 1.5 µg/mL TN for 24 h. (**e**) Quantification of signals in Western blots for CdcD and PDI bands. Data correspond to the quotient of CdcD or PDI divided by EHD signals and normalized to corresponding signals in Ax3. Results are the mean and s.e.m. of three and five independent experiments for CdcD and PDI, respectively (not significant, ns: $P > 0.05$, $^{*}P < 0.05$, $^{**}P < 0.01$, $^{****}P < 0.0001$).

FIGURE 7 *D. discoideum* Δ*sey1* is defective for intracellular replication of *L. pneumophila* and rough ER recruitment.

(**a**) *D. discoideum* Ax3 or Δ*sey1* producing GFP (pDM317) were infected (MOI 1) with (filled symbols) mCherry-producing *L. pneumophila* JR32 or (empty symbols) Δ*icmT* (pNP102) for 6 days. Intracellular replication of the bacteria was assessed by colony-forming units (CFU), of which the number of CFU per mL was calculated and plotted. Data represent mean ± SD of two independent experiments in technical triplicates ($^{***}P < 0.001$). (**b**) *D. discoideum* Ax3 or Δ*sey1* producing GFP (pDM317) were infected (MOI 50) with mCherry-producing *L. pneumophila* Δ*icmT* (pNP102) for the time indicated. Percentage of surviving bacteria was derived from CFU. Data represent mean ± SD of two independent experiments in technical triplicates (not significant, ns: $P > 0.05$). (**c**) *D. discoideum* Ax3 or Δ*sey1*

For Peer Review

producing GFP (pDM317) or Δ*sey1* expressing GFP-Sey1 (pBS001) were infected (MOI 10) for 2 h or 8 h with mCherry-producing *L. pneumophila* JR32 (upper panels) or Δ*icmT* (lower panels). Samples were fixed, stained with uranyl acetate, embedded in Epon/Araldite and analyzed by electron microscopy. Star: *L. pneumophila*; arrowhead: rough endoplasmic reticulum (ER). Scale bars, 500 nm.

FIGURE 8 *D. discoideum* Δ*sey1* cells are impaired for LCV expansion.

(**a**) Representative confocal fluorescence micrographs of dually labeled *D. discoideum* Ax3 (upper panel) or Δ*sey1* mutant (lower panel) producing calnexin-GFP (CnxA-GFP) and P4C-mCherry, infected (MOI 5, 2 h) with mCerulean-producing *L. pneumophila* JR32 (pNP99). Scale bars, 3 µm. (**b**) Imaging flow cytometry (IFC) analysis of dually labelled *D. discoideum* Ax3 and Δ*sey1* mutant producing calnexin-GFP (CnxA-GFP) and P4C-mCherry, infected (MOI 5) with mPlum-producing *L. pneumophila* JR32 (pAW014). Representative images at 6 h p.i. are depicted; scale bars, 7 µm (top panel). Quantification of CnxA-GFP or P4C-mCherry localizing to LCVs during early time points of infection (bottom panel). Number of events per sample, n = 111-1565. Data represent mean ± SD of three independent experiments (*$P < 0.05$, ***$P < 0.001$). (**c**) Representative confocal fluorescence micrographs of dually labeled *D. discoideum* Ax3 (upper panels) or Δ*sey1* mutant (lower panels) producing CnxA-GFP and P4C-mCherry, infected (MOI 5) with mCerulean-producing *L. pneumophila* JR32 (pNP99) for 2 h, 8 h, 16 h or 24 h. Scale bars, 3 µm. (**d**) Quantification of (C) LCV area at the analyzed time points (n = 100). Data represent mean ± 95% CI of three independent experiments (***$P < 0.001$).

For Peer Review

SUPPORTING INFORMATION

FIGURE S1 Confocal microscopy analysis of the ER morphology upon ectopic production of GFP-Sey1, GFP-Sey1_K154A or GFP-Rtnlc.

FIGURE S2 Confocal microscopy analysis of Sec22b, Ufe1 and Use1 localization.

FIGURE S3 Confocal microscopy analysis of intracellular compartments and microtubule architecture.

FIGURE S4 Confocal microscopy analysis of PtdIns(3)*P* and PtdIns(4)*P* localization and actin protrusions.

FIGURE S5 Analysis of lysosomal enzyme secretion, carbohydrate processing and acidification of endocytic compartments.

FIGURE S6 *D. discoideum* Δ*sey1* cells are defective for intracellular replication of *L. pneumophila* and LCV expansion.

FIGURE S7 Schematic representation of the strategies followed for genetic inactivation of *sey1* or *rtnlc*, and PCR-based validation.

TABLE S1 Strains and plasmids used in this study.

TABLE S2 Oligonucleotides used in this study.

For Peer Review

TABLE S3 Antibodies used in this study.

MOVIE S1 Time-lapse video microscopy analysis of Ax3 cells producing the ER marker, GFP-calnexin. Images were taken every second for 2 min.

MOVIE S2 Time-lapse video microscopy analysis of Δ*sey1* cells producing the ER marker, GFP-calnexin. Images were taken every second for 2 min.

MOVIE S3 Time-lapse video microscopy analysis of Ax3 cells producing the cytoskeleton protein tubulin A, GFP-TubA. Images were taken every second for 2 min.

MOVIE S4 Time-lapse video microscopy analysis of Δ*sey1* cells producing the cytoskeleton protein tubulin A, GFP-TubA. Images were taken every second for 2 min.

For Peer Review

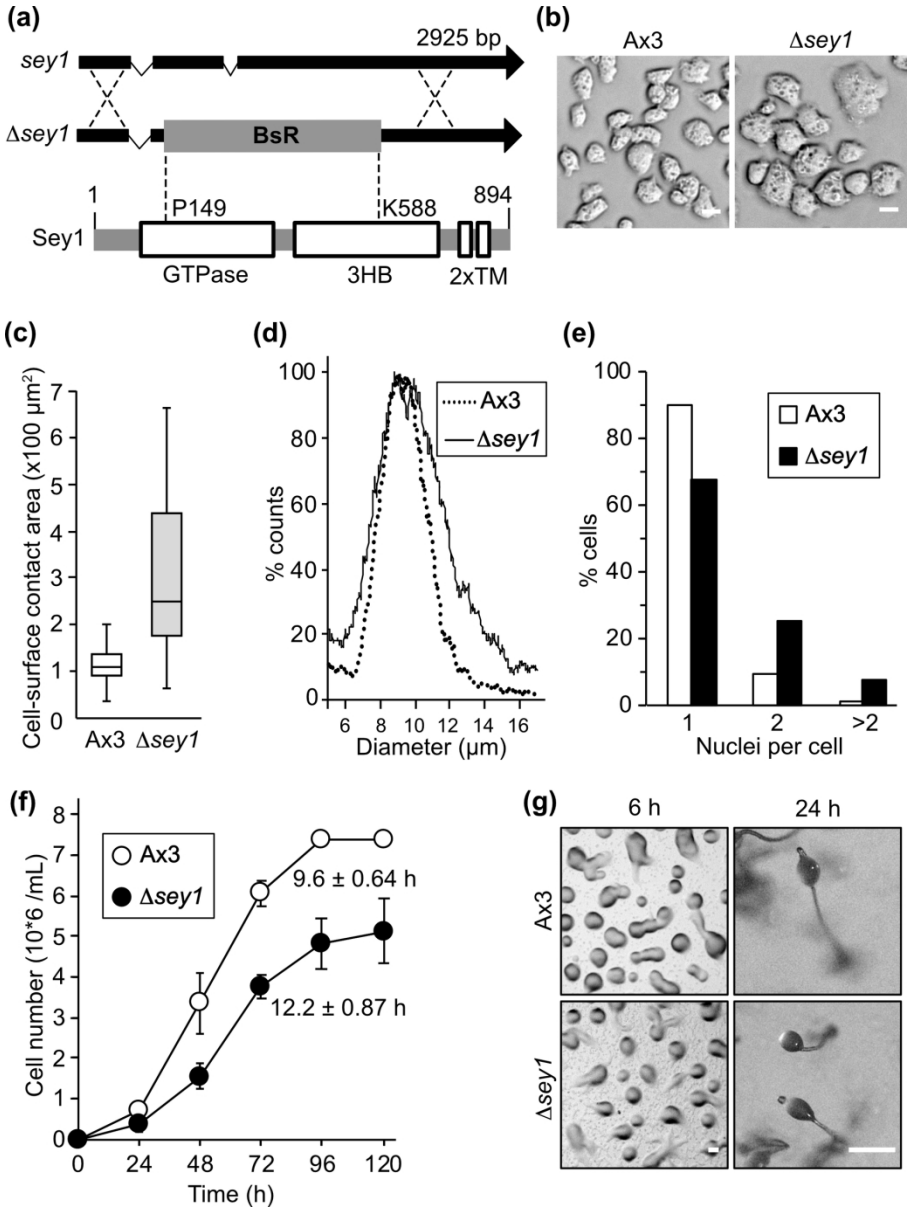

Figure 1

162x215mm (300 x 300 DPI)

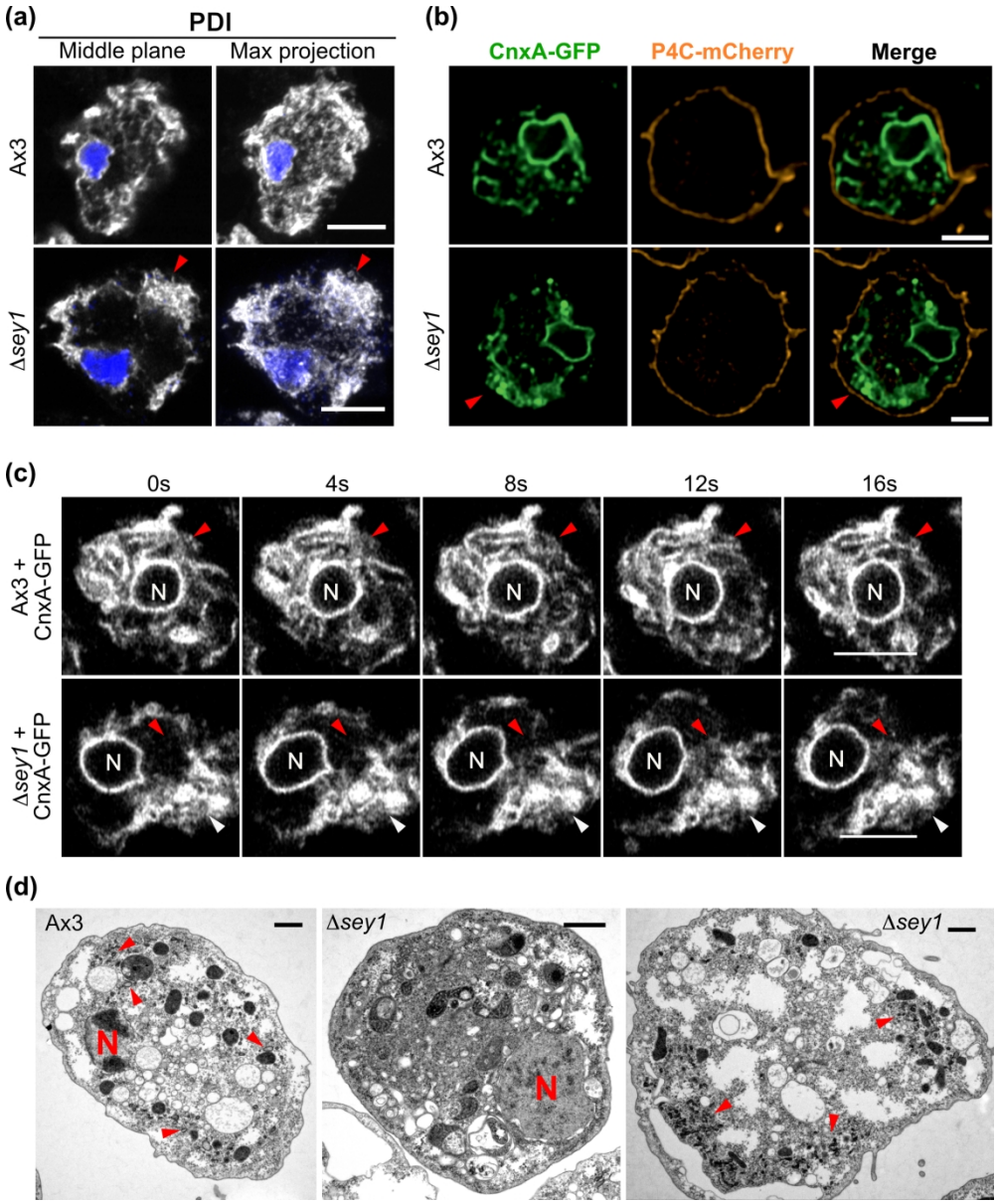

Figure 2

186x225mm (300 x 300 DPI)

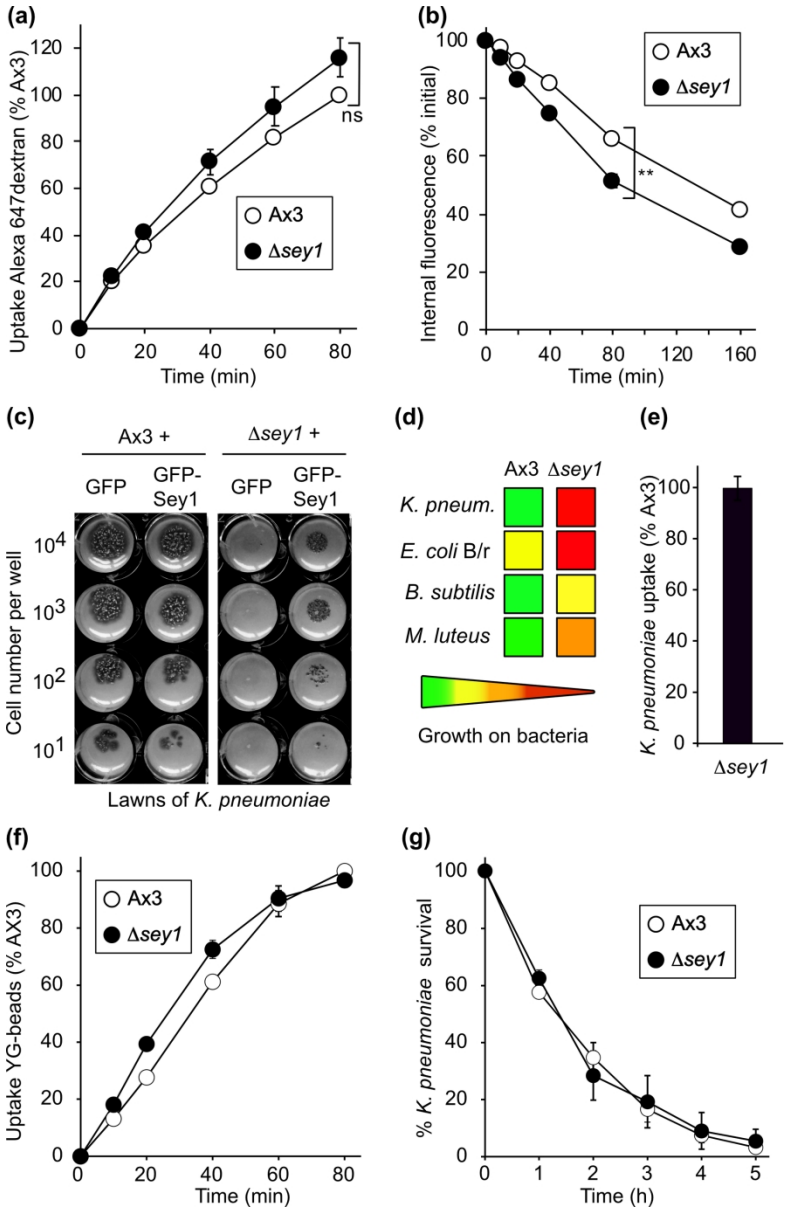

Figure 3

162x250mm (300 x 300 DPI)

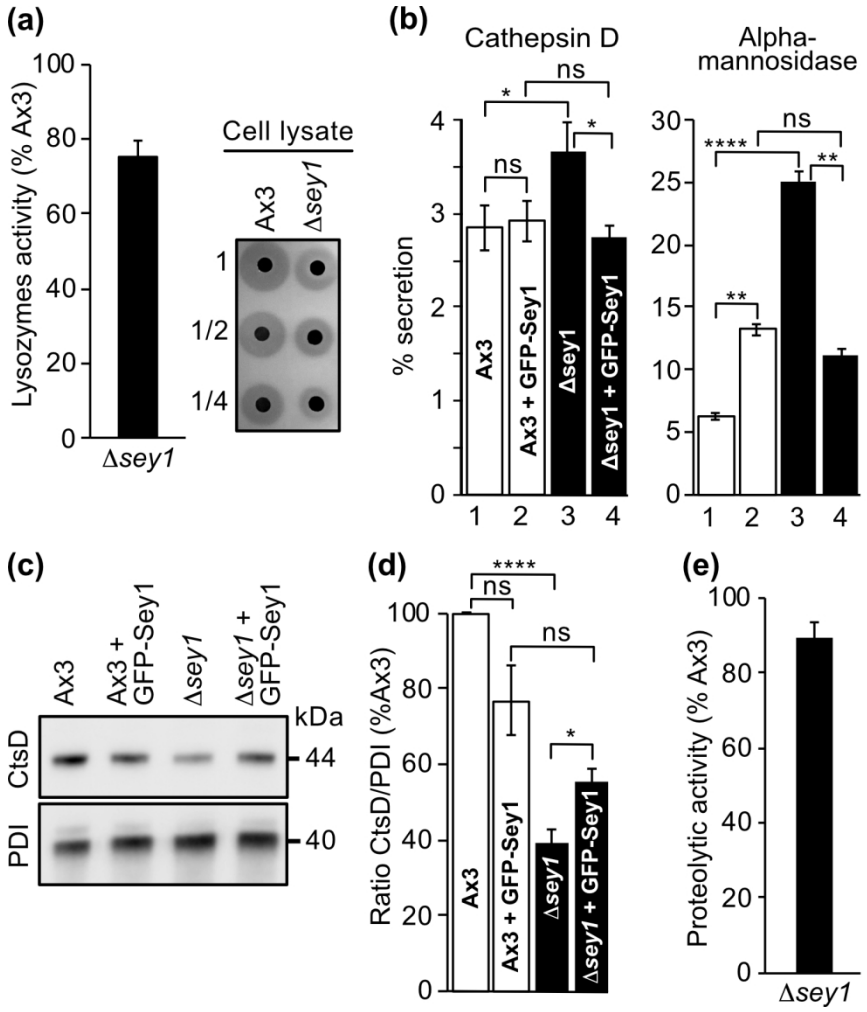
(a)
Lysozymes activity (% Ax3)
100
80
60
40
20
0
Δsey1
Cell lysate
Ax3
Δsey1
1
1/2
1/4
(b)
Cathepsin D
Alpha-mannosidase
% secretion
ns
*
**
****
Ax3
Ax3 + GFP-Sey1
Δsey1
Δsey1 + GFP-Sey1
(c)
Ax3
Ax3 + GFP-Sey1
Δsey1
Δsey1 + GFP-Sey1
kDa
CtsD
PDI
44
40
(d)
Ratio CtsD/PDI (%Ax3)
(e)
Proteolytic activity (% Ax3)

Figure 4

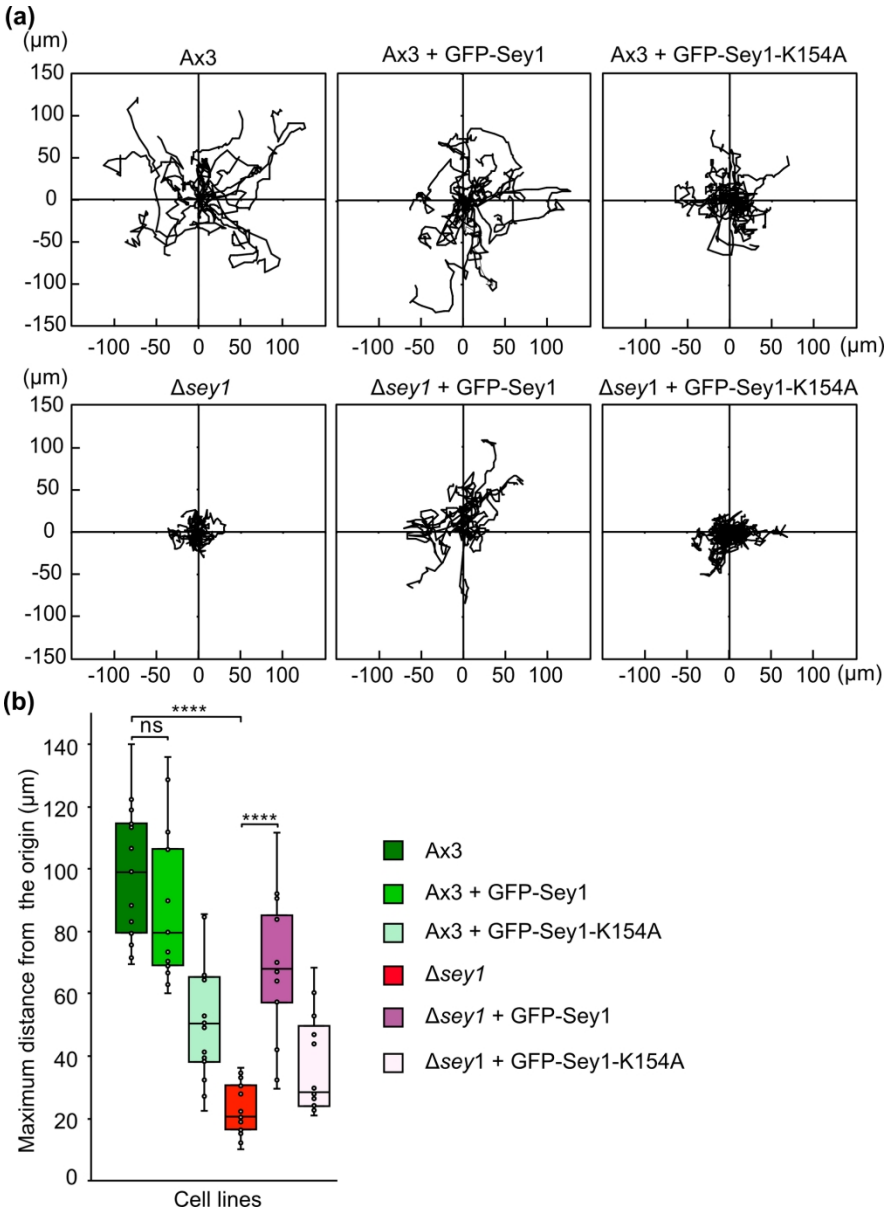

Figure 5

171x233mm (300 x 300 DPI)

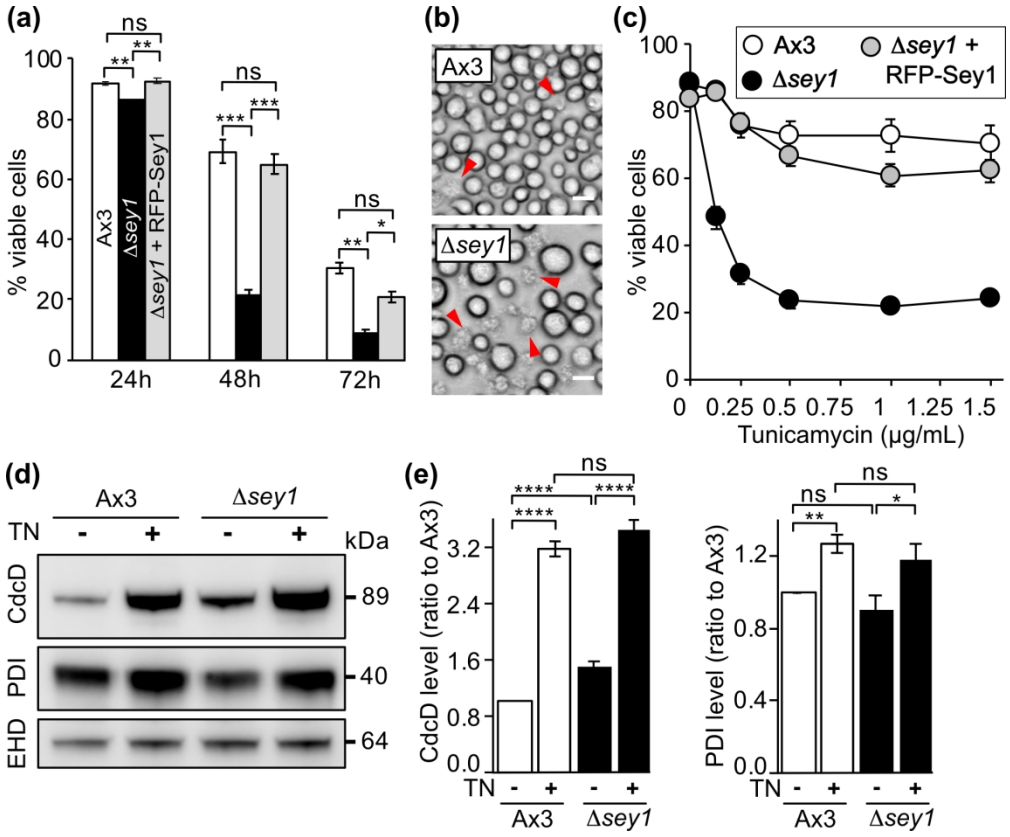
(a)
% viable cells
Ax3
Δsey1
Δsey1 + RFP-Sey1
24h
48h
72h
ns
**
***
*
(b)
Ax3
Δsey1
(c)
Ax3
Δsey1
Δsey1 + RFP-Sey1
% viable cells
Tunicamycin (µg/mL)
(d)
Ax3
Δsey1
TN
kDa
CdcD
PDI
EHD
89
40
64
(e)
CdcD level (ratio to Ax3)
PDI level (ratio to Ax3)
****

Figure 6

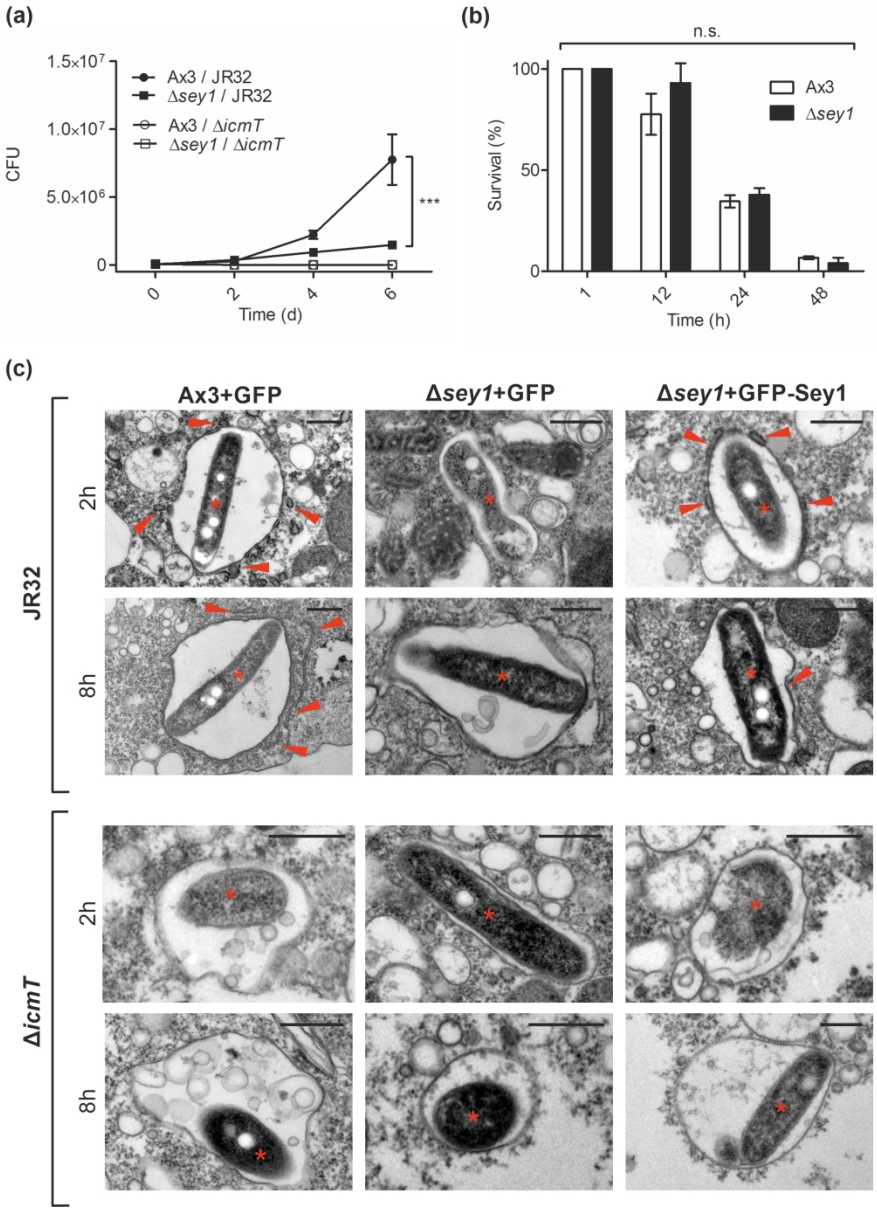
(a)
1.5×10^7
1.0×10^7
5.0×10^6
0
CFU
Ax3 / JR32
Δsey1 / JR32
Ax3 / ΔicmT
Δsey1 / ΔicmT
***
0
2
4
6
Time (d)
(b)
n.s.
100
50
0
Survival (%)
Ax3
Δsey1
1
12
24
48
Time (h)
(c)
Ax3+GFP
Δsey1+GFP
Δsey1+GFP-Sey1
JR32
2h
8h
ΔicmT
2h
8h

Figure 7

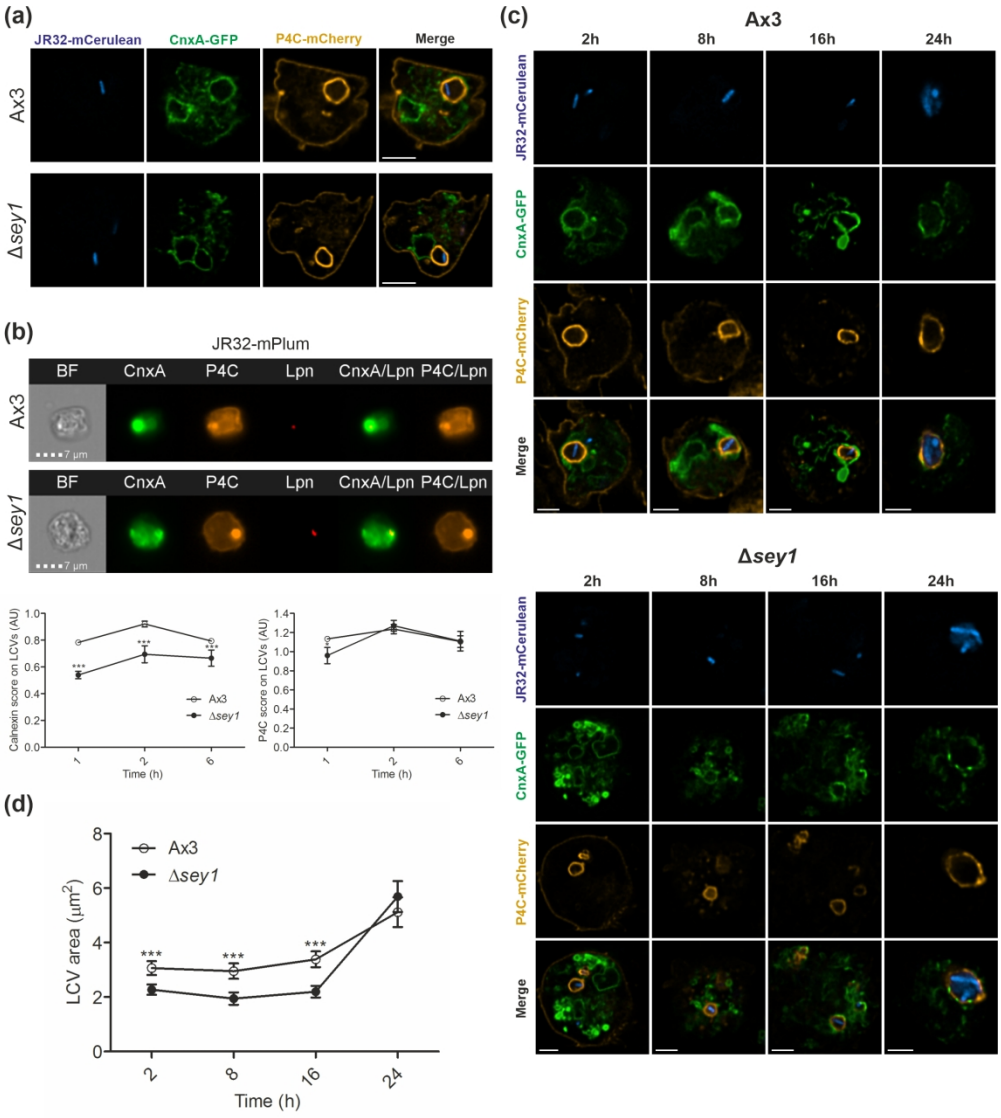
(a)
JR32-mCerulean
CnxA-GFP
P4C-mCherry
Merge
Ax3
Δsey1
(b)
JR32-mPlum
BF
CnxA
P4C
Lpn
CnxA/Lpn
P4C/Lpn
Ax3
Δsey1
7 µm
Calnexin score on LCVs (AU)
P4C score on LCVs (AU)
Time (h)
Ax3
Δsey1
(c)
Ax3
2h
8h
16h
24h
JR32-mCerulean
CnxA-GFP
P4C-mCherry
Merge
Δsey1
(d)
LCV area (µm²)
Time (h)
Ax3
Δsey1

Figure 8